

Arbeitsbericht NAB 13-51

**Water and air permeability tests
on deep core samples from
Schlattingen SLA-1 borehole**

June 2013

E. Romero & R. Gómez

Nationale Genossenschaft
für die Lagerung
radioaktiver Abfälle

Hardstrasse 73
CH-5430 Wettingen
Telefon 056-437 11 11

www.nagra.ch

Arbeitsbericht NAB 13-51

**Water and air permeability tests
on deep core samples from
Schlattingen SLA-1 borehole**

June 2013

E. Romero & R. Gómez

KEYWORDS

Schlattingen, petrophysics, laboratory tests, gas tests,
water tests, rock physics, mineralogy, porosimetry

**Nationale Genossenschaft
für die Lagerung
radioaktiver Abfälle**

Hardstrasse 73
CH-5430 Wettingen
Telefon 056-437 11 11

www.nagra.ch

Nagra Working Reports concern work in progress that may have had limited review. They are intended to provide rapid dissemination of information. The viewpoints presented and conclusions reached are those of the author(s) and do not necessarily represent those of Nagra.

"Copyright © 2013 by Nagra, Wettingen (Switzerland) / All rights reserved.

All parts of this work are protected by copyright. Any utilisation outwith the remit of the copyright law is unlawful and liable to prosecution. This applies in particular to translations, storage and processing in electronic systems and programs, microfilms, reproductions, etc."

Table of Contents

| | |
|--|------------|
| Table of Contents | I |
| List of Tables | II |
| List of Figures..... | III |
| 1 Introduction | 1 |
| 1.1 Background and Scope | 1 |
| 1.2 The geothermal well Schlattingen-1 | 2 |
| 2 Materials used in the Research..... | 7 |
| 2.1 General characterisation and initial conditions..... | 7 |
| 2.2 Pore size distribution | 9 |
| 2.3 Specimen preparation | 14 |
| 2.4 Artificial pore water preparation | 16 |
| 2.5 Water retention curve | 17 |
| 2.6 Equipment, experimental set-up and test procedure..... | 20 |
| 3 Test Results | 27 |
| 3.1 Compressibility on mean stress and pore pressure changes | 27 |
| 3.2 Water permeability results - time evolution of water volume change | 32 |
| 3.3 Air injection results | 42 |
| 4 Summary and Conclusions | 51 |
| 5 References..... | 53 |

List of Tables

| | | |
|-----------|--|----|
| Tab. 1-1: | Important technical borehole information about the geothermal well Schlattingen-1..... | 5 |
| Tab. 2-1: | Samples received at the Geotechnical Laboratory (UPC). | 7 |
| Tab. 2-2: | Initial conditions of tested samples..... | 8 |
| Tab. 2-3: | Initial conditions of shallow samples (Romero et al. 2012b,c) and deep OPA samples (this study). | 9 |
| Tab. 2-4: | Properties of Artificial Pore Water (APW)..... | 17 |
| Tab. 3-1: | Different loading/unloading stages followed on both materials for the water permeability determinations. | 31 |
| Tab. 3-2: | Water permeability results..... | 41 |

List of Figures

| | | |
|---------------|---|----|
| Fig. 1-1: | Topographic map, displaying the location of the geothermal well Schlattingen-1 (SLA-1). | 2 |
| Fig. 1-2: | Stratigraphy of the geothermal well Schlattingen-1 (SLA-1) after Albert et al. (2012). | 4 |
| Fig. 2-1: | Cylindrical sample of 'Brown Dogger' OED 20/Harz (776.51 – 776.72 m) immersed in synthetic pore water and displaying bedding planes orthogonal to the direction of coring. | 7 |
| Fig. 2-2: | Cumulated intruded void ratio (MIP and BJH). 'Brown Dogger' OED 20/Harz (776.51 - 776.72 m). | 10 |
| Fig. 2-3: | PSD functions with dominant pore modes (MIP and BJH). 'Brown Dogger' OED 20/Harz (776.51 - 776.72 m). | 11 |
| Fig. 2-4: | Cumulated intruded void ratio (MIP and BJH). OPA OED (879.79 - 880.01 m). | 11 |
| Fig. 2-5: | PSD functions with dominant pore modes (MIP and BJH). OPA OED (879.79 - 880.01 m). | 12 |
| Fig. 2-6: | Cumulated intruded void ratio (MIP and BJH). 'Brown Dogger' OED 20/Harz (776.51 - 776.72 m) and OPA OED (879.79 - 880.01 m). | 13 |
| Fig. 2-7: | PSD functions with dominant pore modes (MIP and BJH). 'Brown Dogger' OED 20/Harz (776.51 - 776.72 m) and OPA OED (879.79 - 880.01 m). | 13 |
| Fig. 2-8: | Cumulated intruded void ratio (left) and PSD functions with dominant pore modes (right). Deep (879.9 m) and shallow (300 m) OPA samples. | 14 |
| Fig. 2-9: | Steps followed to prepare specimen (50.0 mm in diameter and 25.4 mm high). (a) Pre-cutting a slice of the core sample under dry conditions with a band saw. | 14 |
| Fig. 2-9cont: | Steps followed to prepare specimen: (b) Preparing the circular cross-section (50.0 mm in diameter) with a lathe under dry conditions. | 15 |
| Fig. 2-9cont: | Steps followed to prepare specimen (cont): finishing (c) and sealing of the samples. | 16 |
| Fig. 2-10: | Water retention curve. Sample OED 20/Harz (776.51 - 776.72 m). | 18 |
| Fig. 2-11: | Water retention curve. Sample OED (879.79 - 880.01 m). | 18 |
| Fig. 2-12: | Water retention curve. Comparison between OED 20/Harz (776.51 - 776.72 m) and OED (879.79 - 880.01 m) samples. | 19 |
| Fig. 2-13: | Water retention curves of OPA samples. Left: 'Shallow sample' (BHA-8/1; approx. 300 m depth). Right: 'Deep sample' (OED 879.9 m depth). | 19 |
| Fig. 2-14: | Overview of the instrumented high-pressure triaxial cell. | 21 |
| Fig. 2-15: | Cross-section of the high-pressure triaxial cell. | 21 |
| Fig. 2-16: | Scheme of the air injection and water permeability setup with high-pressure triaxial cell and four pressure/volume controllers (two for air and two for water). | 22 |

| | | |
|------------|---|----|
| Fig. 2-17: | Type of tests followed during controlled-gradient water permeability tests and fast air injection tests followed by recovery period at constant volume. | 23 |
| Fig. 2-18: | Steps followed during sample installation in the triaxial cell. | 23 |
| Fig. 3-1: | Compression curves during isotropic loading from 0.1 to 10 MPa at constant water content for OED 20/Harz 'Brown Dogger' at 776.51 - 776.72 m, and deep OED Opalinus Clay at 879.79 - 880.01 m. | 27 |
| Fig. 3-2: | Swelling (negative strains correspond to swelling) during water pressure application (flooding) at constant $p = 10$ MPa for OED 20/Harz 'Brown Dogger' at 776.51 - 776.72 m, and deep OED Opalinus Clay at 879.79 - 880.01 m. | 28 |
| Fig. 3-3: | Axial strain evolution during p change from 10 to 11.75 MPa and u_w change (bottom cap) from 2 to 5.5 MPa. OED 20/Harz 'Brown Dogger' at 776.51 - 776.72 m, and deep OED Opalinus Clay at 879.79 - 880.01 m. | 29 |
| Fig. 3-4: | Axial strain evolution during p change from 11.75 to 13.25 MPa and u_w change (bottom cap) from 5.5 to 8.5 MPa. OED 20/Harz 'Brown Dogger' at 776.51 - 776.72 m, and deep OED Opalinus Clay at 879.79 - 880.01 m. | 29 |
| Fig. 3-5: | Axial strain evolution during p change from 13.25 to 15 MPa and at constant $u_w = 8.5$ MPa (bottom cap). OED 20/Harz 'Brown Dogger' at 776.51 - 776.72 m, and deep OED Opalinus Clay at 879.79 - 880.01 m. | 30 |
| Fig. 3-6: | Axial strain evolution at constant $p = 15$ MPa and u_w change (bottom cap) from 8.5 to 0.5 MPa. OED 20/Harz 'Brown Dogger' at 776.51 - 776.72 m, and deep OED Opalinus Clay at 879.79 - 880.01 m. | 30 |
| Fig. 3-7: | Time evolution of water inflow / outflow volumes. Stage at $p = 10$ MPa; $u_{wbottom} = 2$ MPa; $u_{wtop} = 0.5$ MPa. OED 20/Harz 'Brown Dogger' sample. | 32 |
| Fig. 3-8: | Time evolution of water inflow / outflow volumes. Stage at $p = 11.75$ MPa; $u_{wbottom} = 5.5$ MPa; $u_{wtop} = 0.5$ MPa. OED 20/Harz 'Brown Dogger' sample. | 33 |
| Fig. 3-9: | Time evolution of water inflow volume. Stage at $p = 13.25$ MPa; $u_{wbottom} = 8.5$ MPa; $u_{wtop} = 0.5$ MPa. OED 20/Harz 'Brown Dogger' sample. | 33 |
| Fig. 3-10: | Time evolution of water inflow volume. Stage at $p = 15.0$ MPa; $u_{wbottom} = 8.5$ MPa; $u_{wtop} = 0.5$ MPa. OED 20/Harz 'Brown Dogger' sample. | 34 |
| Fig. 3-11: | Time evolution of $\Delta V_w / (A i \Delta t)$ (three intervals have been considered under steady state conditions). Stage at $p = 10$ MPa; $u_{wbottom} = 2$ MPa; $u_{wtop} = 0.5$ MPa. OED 20/Harz 'Brown Dogger' sample. | 35 |
| Fig. 3-12: | Time evolution of $\Delta V_w / (A i \Delta t)$ under steady state conditions. Stage at $p = 11.75$ MPa; $u_{wbottom} = 5.5$ MPa; $u_{wtop} = 0.5$ MPa. OED 20/Harz 'Brown Dogger' sample. | 35 |
| Fig. 3-13: | Time evolution of $\Delta V_w / (A i \Delta t)$ under steady state conditions. Stage at $p = 13.25$ MPa; $u_{wbottom} = 8.5$ MPa; $u_{wtop} = 0.5$ MPa. OED 20/Harz 'Brown Dogger' sample. | 36 |
| Fig. 3-14: | Time evolution of $\Delta V_w / (A i \Delta t)$ under steady state conditions. Stage at $p = 15.0$ MPa; $u_{wbottom} = 8.5$ MPa; $u_{wtop} = 0.5$ MPa. OED 20/Harz 'Brown Dogger' sample. | 36 |

| | | |
|------------|--|----|
| Fig. 3-15: | Time evolution of water outflow volume. Stage at $p = 11.75$ MPa; $u_{wbottom} = 5.5$ MPa; $u_{wtop} = 0.5$ MPa. OED Opalinus Clay sample..... | 37 |
| Fig. 3-16: | Time evolution of water outflow volume. Stage at $p = 13.25$ MPa; $u_{wbottom} = 8.5$ MPa; $u_{wtop} = 0.5$ MPa. OED Opalinus Clay sample..... | 38 |
| Fig. 3-17: | Time evolution of water outflow volume. Stage at $p = 15.0$ MPa; $u_{wbottom} = 8.5$ MPa; $u_{wtop} = 0.5$ MPa. OED Opalinus Clay sample..... | 38 |
| Fig. 3-18: | Time evolution of $\Delta V_w / (A i \Delta t)$ under steady state conditions. Stage at $p =$ 11.75 MPa; $u_{wbottom} = 5.5$ MPa; $u_{wtop} = 0.5$ MPa. OED Opalinus Clay sample. | 39 |
| Fig. 3-19: | Time evolution of $\Delta V_w / (A i \Delta t)$ under steady state conditions. Stage at $p =$ 13.25 MPa; $u_{wbottom} = 8.5$ MPa; $u_{wtop} = 0.5$ MPa. OED Opalinus Clay sample. | 39 |
| Fig. 3-20: | Time evolution of $\Delta V_w / (A i \Delta t)$ under steady state conditions. Stage at $p =$ 15.0 MPa; $u_{wbottom} = 8.5$ MPa; $u_{wtop} = 0.5$ MPa. OED Opalinus Clay sample. | 40 |
| Fig. 3-21: | Water permeability as a function of void ratio: OED 20/Harz (776.51 - 776.72 m) and OED (879.79 - 880.01 m) samples. Dependency on void ratio and orientation effects on shallow OPA samples. | 41 |
| Fig. 3-22: | Water permeability dependency on void ratio for flow perpendicular to bedding. 'Deep samples': OED 20/Harz (776.51 - 776.72 m) and OED (879.79 - 880.01 m). 'Shallow samples': OPA BHA-8/1 (approx. 300 m depth)..... | 42 |
| Fig. 3-23: | Measured time evolution of pressures at the injection and outflow sides together with outflow volume and axial displacements. OPA shallow sample with bedding plane orientation orthogonal to flow at $p = 15$ MPa. | 44 |
| Fig. 3-24: | Measured time evolution of pressures at the injection and outflow sides together with outflow volume and axial displacements. 'Shallow sample' with bedding plane orientation parallel to flow at $p = 15$ MPa. | 44 |
| Fig. 3-25: | Axial strain changes associated with constitutive (effective) stress changes during air tests with flow parallel and orthogonal to bedding. | 45 |
| Fig. 3-26: | Measured time evolution of pressures at the injection and outflow sides together with outflow volume and axial displacements. OED 20/Harz 'Brown Dogger' (776.51 - 776.72 m) sample with flow orthogonal to bedding plane orientation at $p = 15$ MPa. | 46 |
| Fig. 3-27: | Measured time evolution of pressures at the injection and outflow sides together with outflow volume and axial displacements. OED 20/Harz 'Brown Dogger' (776.51 - 776.72 m) sample with flow orthogonal to bedding plane orientation at $p = 19$ MPa. | 46 |
| Fig. 3-28: | Measured time evolution of pressures at the injection and outflow sides together with outflow volume and axial displacements. OED Opalinus Clay (879.79 - 880.01 m) sample with flow orthogonal to bedding plane orientation at $p = 15$ MPa. | 47 |
| Fig. 3-29: | Measured time evolution of pressures at the injection and outflow sides together with outflow volume and axial displacements. OED Opalinus Clay (879.79 - 880.01 m) sample with flow orthogonal to bedding plane orientation at $p = 19$ MPa. | 48 |

Fig. 3-30: Axial strain changes associated with constitutive (effective) stress changes during air tests with flow orthogonal to bedding. Samples of OED Opalinus Clay (879.79 - 880.01 m) and OED 20/Harz 'Brown Dogger' (776.51 - 776.72 m) at (a) $p = 15$ MPa and (b) $p = 19$ MPa..... 49

1 Introduction

1.1 Background and Scope

The Department of Geotechnical Engineering and Geosciences of the Universitat Politècnica de Catalunya in Barcelona (UPC) was requested by NAGRA to perform a geomechanical testing program on two core samples extracted from a deep geothermal well near the village of Schlattingen in the Molasse Basin of Northern Switzerland. The laboratory studies are aimed at characterising the fluid and gas transport behavior of two candidate host rock formations for the disposal of radioactive waste, namely the so-called 'Brown Dogger' (stratigraphic sequence of Callovian, Bathonian and Bajocian age) and the Opalinus Clay. The investigation programme comprises basic geotechnical identification tests, determination of the water retention behaviour and water / gas permeability tests in a triaxial cell. The results of the laboratory investigations will feed in Nagra's data base on gas related host rock properties. The electronic data base is enclosed in Appendix A.

The initial characterisation program included the definition of the initial state of the tested materials (water content, dry density, density of solids, initial suction, and pore size density function with mercury intrusion porosimetry MIP / nitrogen adsorption). The first stage of the program was intended to provide quantitative data to calibrate hydraulic and two-phase flow properties through MIP (pore size distribution assimilated to water retention curve), water retention tests (psychrometer measurements), as well as water permeability tests at different (effective) stress states and hydraulic gradients that allowed accounting for the change in permeability with void ratio. The different stress states were attained after isotropic compression under controlled confining stress rate and specified water back-pressure. These tests also allowed determining compressibility on loading/unloading of the intact material. The main stage of the program was devoted to study the influence of the stress state under isotropic conditions on the air permeability of initially water saturated samples. Four controlled-volume rate air injection experiments were performed in a triaxial cell by testing two different rock samples under two isotropic stress states (flow was always orthogonal to bedding planes). Two different maximum air injection pressures were attained at high and constant air injection rate (100 mL/min) before shut-in and air dissipation. The maximum air injection pressures were in one case below the air-entry value determined by MIP and around the air-entry value in the second case. Particular emphasis was placed in monitoring sample volume changes (axial strains) during air injection and dissipation stages. Tests were performed during July 2011 and July 2012.

The present report includes the following information for each rock type:

- Documentation of sample and synthetic pore water preparations, experimental set-up and detailed water and air test protocols followed.
- Definition of the initial state (water content, dry density, density of solids and initial suction), as well as mercury intrusion porosimetry / nitrogen adsorption tests and water retention results (psychrometer measurements during main drying starting from initial conditions).
- Controlled stress rate isotropic compression results under controlled water pressure and their corresponding compressibility.

- Water permeability determined at four different stress states (total stresses of 10, 11.75, 13.25 and 15 MPa), which will be used to assess the void ratio dependence on water permeability. Constant backpressure conditions (downstream between 0.5 and 2 MPa and upstream between 2 and 8.5 MPa) were used to determine water permeability under steady state conditions and flow orthogonal to bedding planes.
- Air permeability results at two different maximum air injection pressures (below the air-entry value determined by MIP at a maximum air pressure of 14 MPa and around the air-entry value at 18 MPa). Time evolution of upstream and downstream pressures, as well as outflow volume and sample volume changes, during the injection and dissipation stages. There was no post-mortem sample characterisation after finishing the air tests.

1.2 The geothermal well Schlattingen-1

The two core samples were recovered by Nagra from the geothermal well Schlattingen-1 (SLA-1) at two different depths (776.5 m depth 'Brown Dogger' (BD) and 879.9 m depth Opalinus Clay (OPA)). The geothermal well SLA-1 is located on the road between Basadingen, Schlattingen and Diessenhofen (Canton Thurgau) about 10 km south-east of the town Schaffhausen (approx. N 47°40'41.7", E 8°45'42"; 416.6 m asl) in the Northeastern part of the Swiss Molasse Basin (Figure 1-1). The borehole is intended to produce geothermal energy for an economical and CO₂-emission-free operation of greenhouses. Therefore, during 2011, a first deep borehole Schlattingen-1 was drilled to use the ground water from aquifers in the Upper Muschelkalk and the transition Mesozoic / permo-carboniferous - crystalline rocks. The borehole reached a final depth of 1508 m, passed through the Quaternary, Tertiary, Jurassic and Triassic sediment sequence (with marls, silt-, sand-, and claystones, limestones) and finally encountered the crystalline basement (Albert et al. 2012).



Fig. 1-1: Topographic map, displaying the location of the geothermal well Schlattingen-1 (SLA-1).

The drilling of borehole Schlattingen-1 was accompanied by an extensive site characterization program, including lithostratigraphic and structural mapping of drillcores in the clay-rich Mesozoic sequences, geophysical logging, hydraulic packer testing, water sampling and hydraulic fracturing stress measurements. Focus of the investigations was on the geological and geotechnical characterisation of the candidate host rock formations, namely the Effingen Member, the so-called 'Brown Dogger' (stratigraphic sequence of Callovian, Bathonian and Bajocian age) and the Opalinus Clay. The stratigraphic profile of borehole Schlattingen-1 is shown in Figure 1-2, available technical borehole data are summarized in Table 1-1.

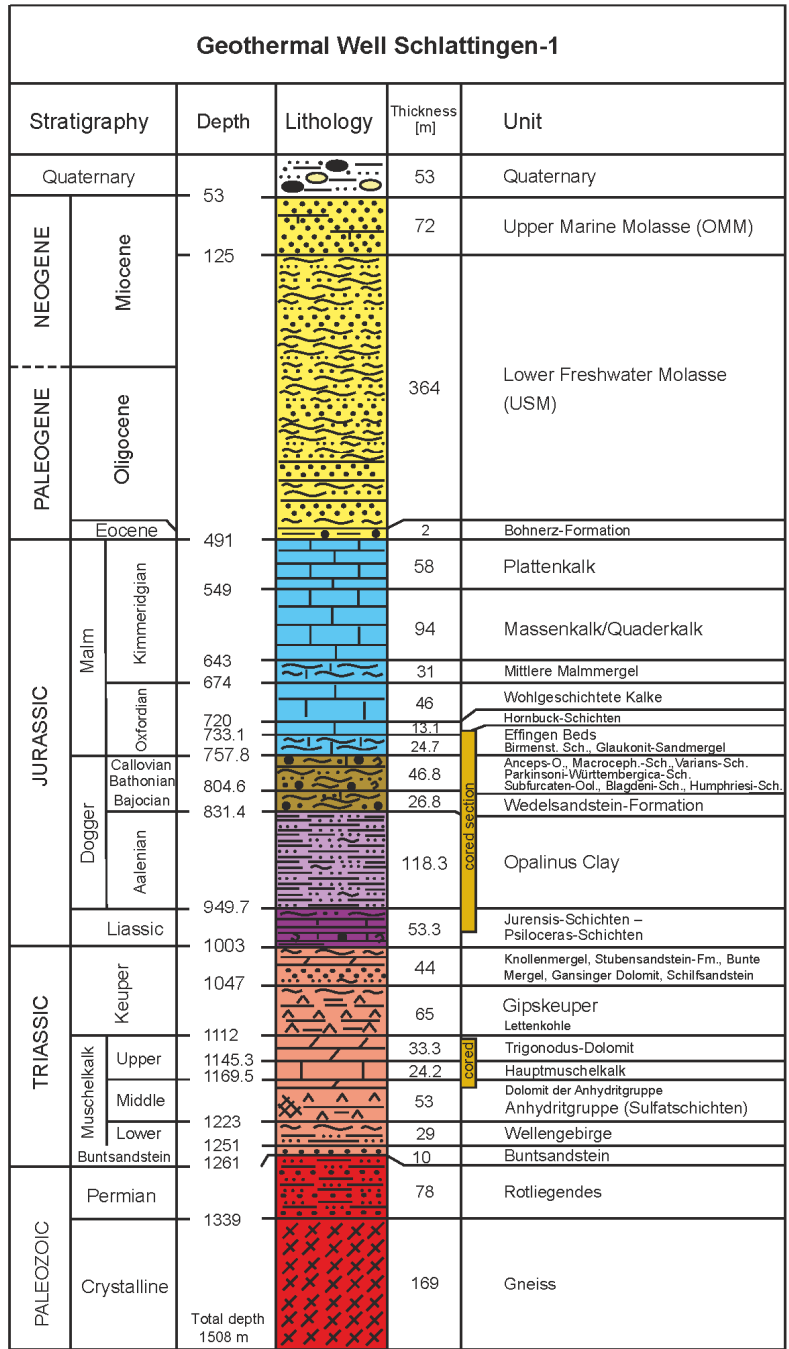


Fig. 1-2: Stratigraphy of the geothermal well Schlattungen-1 (SLA-1) after Albert et al. (2012).

Tab. 1-1: Important technical borehole information about the geothermal well Schlattingen-1.

| Geothermal Well Schlattingen-1 – SLA-1 | | |
|--|--|---|
| Location | Village of Schlattingen, around 10 km south-east of Schaffhausen | |
| Co-ordinates | N 47°40'41.7", E 8°45'42" | |
| Elevation | 416.6 m asl | |
| Max. depth: | 1508.0 bg | |
| Drilling techniques | Percussion drilling, cuttings: | 0 - 725 m bg 989 - 1116 m bg 1185 - 1508 m bg |
| | Single barrel core drilling: | 725 - 989 m bg 1116 - 1185 m bg |
| Investigation programme | Petrophysical logging: | GR, FEL, DIL, DLL, Gamma-Gamma, Neutron-Neutron, Sonic) |
| | Core mapping / structural logging: | ABF, ABI |
| | Packer Testing: | 4 Tests |
| | Hydrofracturing: | 15 Tests |
| | Porewater sampling: | 4 Samples |
| | Mineralogical and geotechnical characterization of core samples | (> 50 samples tested) |

2 Materials used in the Research

2.1 General characterisation and initial conditions

Core samples were retrieved by Nagra from the deep geothermal well SLA-1 near the village of Schlattingen (Fig. 1-1). Samples correspond to a clay-rich sequence called 'Brown Dogger' (Parkinsoni-Württembergica strata of the Upper Dogger) and from the deeper Opalinus Clay (OPA) formation (Fig. 1-2). The OPA sequence starts at 831.4 m bg. The cores were recovered with a double core barrel using a NaCl drilling mud. After on-site core documentation, the 100-mm diameter samples were cast immediately in epoxy resin and placed inside PVC tubes for save preservation during shipment. A total of four core-samples were received at the Geotechnical Laboratory (UPC), which are detailed in Table 2-1.

Tab. 2-1: Samples received at the Geotechnical Laboratory (UPC).

| Sequence and core-sample reference | Depth (m) | Date (core preservation) | Observations / Remarks |
|------------------------------------|-----------------|--------------------------|--|
| 'Brown Dogger' OED 20/Harz | 776.51 - 776.72 | 21/03/2011 | |
| 'Brown Dogger' EMPA SLA | 781.55 - 781.85 | 21/03/2011 | Repeated resin impregnation; first trial not successful (resin did not harden) |
| OPA / OED | 879.79 - 880.01 | 17/04/2011 | |
| OPA / OED 1/1 | 936.26 - 936.49 | 10/06/2011 | |



Fig. 2-1: Cylindrical sample of 'Brown Dogger' OED 20/Harz (776.51 – 776.72 m) immersed in synthetic pore water and displaying bedding planes orthogonal to the direction of coring.

The main geotechnical properties of the studied core-samples 'Brown Dogger' OED 20/Harz (776.51 – 776.72 m) and OPA / OED (879.79 – 880.01 m) are summarised in Table 2-2. The information is complemented with the initial total suction ψ measured with dew point mirror psychrometer (Cardoso *et al.* 2007). The sample size used in the experimental program was 50.0 mm in diameter and 25.4 mm height, with axis parallel to coring and orthogonal to bedding planes (Fig. 2-1).

Tab. 2-2: Initial conditions of tested samples.

| Sequence / formation | 'Brown Dogger' | Opalinus Clay |
|--|---|---|
| Core-sample reference | OED 20/Harz (776.51 – 776.72 m) | OED (879.79 – 880.01 m) |
| Density, ρ (Mg/m ³) | 2.51 | 2.53 |
| Water content, w (%) | 4.34 – 5.43 | 4.30 – 4.70 |
| Density of solids, ρ_s (Mg/m ³) | 2.69 | 2.69 |
| Dry density, ρ_d (Mg/m ³) | 2.38 – 2.41 | 2.42 – 2.43 |
| Void ratio, e | 0.116 – 0.130 | 0.107 – 0.112 |
| Porosity, n | 0.104 – 0.115 | 0.097 – 0.101 |
| Degree of saturation, S_r ($\rho_w = 1$ Mg/m ³) | 1.0 | 1.0 |
| Total suction, ψ (MPa) | 5 | 4 |
| Dominant pore mode from MIP (nm) | 20 | 16 |
| Air-entry value from MIP (MPa) | 13 | 18 |
| van Genuchten p_0 (MPa) | 18 | 27 - 34 |
| van Genuchten n poresize parameter (-) | 1.58 | 1.58 |
| Liquid limit, w_L (%) | 28 | 38±5* |
| Plastic limit, w_P (%) | 18 | 23±2* |
| Mineralogy** (%) | Clay: 34-52 Quartz: 24-30 Carb.: 20-33 (Parkinsoni-Württembergica) | Clay: 55 Quartz: 26 Carb.: 17 (sample: SLA-18: 880.30 m) |

* Shaly facies, approx. 300 m depth bg. Core BHA-8/1; MI-niche, Mont Terri Underground Rock Laboratory in Jura Mountains (North-western Switzerland).

** Mineralogical composition taken from Nagra's mineralogical data base (Mazurek 2011).

Table 2-3 shows a comparison between the initial conditions of OPA shallow samples BHG-D1 (10.2-11 m) and BHA-8/1, both approximately at 300 m depth bg in the shaly facies (HG experiment layout and MI-niche at Mont Terri Underground Rock Laboratory in North-western Switzerland, respectively) and the deep OPA sample used in the present research (see also Romero et al., 2012b, c).

Tab. 2-3: Initial conditions of shallow samples (Romero et al. 2012b,c) and deep OPA samples (this study).

| Property | OPA shallow sample BHG-D1 10.2-11 m (approx. 300 m depth) | OPA shallow sample BHA-8/1 MI-niche (approx. 300 m depth) | OPA OED (879.9 m depth) |
|--|---|---|-------------------------|
| Density, ρ (Mg/m ³) | 2.32 | 2.34 - 2.38 | 2.53 |
| Water content, w (%) | 7.85 | 6.60 – 6.90 | 4.30 – 4.70 |
| Density of solids, ρ_s (Mg/m ³) | 2.69 | 2.70 | 2.69 |
| Dry density, ρ_d (Mg/m ³) | 2.15 | 2.20 – 2.23 | 2.42 – 2.43 |
| Void ratio, e | 0.25 | 0.210 – 0.230 | 0.107 – 0.112 |
| Porosity, n | 0.20 | 0.170 – 0.190 | 0.097 – 0.101 |
| Degree of saturation, S_r ($\rho_w = 1$ Mg/m ³) | 0.85 | 0.77 - 0.88 | 1.0 |
| Total suction, ψ (MPa) | 24 | 15 | 4 |
| Dominant pore mode from MIP (nm) | 16 | 23 | 16 |
| Air-entry value from MIP (MPa) | 18 | 13 | 18 |
| van Genuchten p_0 (MPa) | - | 18 | 27 - 34 |
| van Genuchten n poresize parameter (-) | - | 1.67 | 1.67 |
| Liquid limit, w_L (%) | 41 | 38±5 | - |
| Plastic limit, w_P (%) | 23 | 23±2 | - |

2.2 Pore size distribution

Mercury intrusion porosimetry tests were carried out on freeze-dried materials to characterise their porosity network (details can be found in Romero & Simms 2008; Romero *et al.* 2012a). Washburn equation may be adopted to provide a relationship between the applied (absolute) mercury pressure p and a characteristic entrance size of the intruded pores x :

$$p = - \frac{4 \sigma_{Hg} \cos \theta_{nw}}{x} \quad (1)$$

where σ_{Hg} is the surface tension of mercury ($\sigma_{Hg} = 0.484$ N/m at 25°C), θ_{nw} the contact angle between mercury and particles surface ($\theta_{nw} = 147^\circ$ maximum value for clay minerals, and usually between 139° and 147°), and x the entrance or throat pore diameter (cylindrical model). Figure 2-2 shows the cumulative intruded pore volume normalised by solid volume (intruded void ratio) plotted against the entrance pore size for 'Brown Dogger' sample. There is some deviation from the initial void ratio (refer to Table 2-2), due to the limited capacity of the porosimeter to enter the smallest pores (non-intruded porosity). Other useful information that can be obtained from the MIP test is the pore size density PSD function (Figure 2-3), defined as:

$$f(\log x) = -de/d(\log x),$$

where x represents the entrance pore size. The PSD function obtained from MIP displays one dominant pore mode at approximately 20 nm for 'Brown Dogger'. The pore network description was complemented by nitrogen adsorption tests. The pore size distribution was estimated following the Barrett, Joyner and Halenda (BJH) method using the desorption information (Webb & Orr 1997). A wider range of pore sizes is covered when using this complementary information. The complementary cumulative intruded pore volume and PSD function obtained by BJH are plotted in Figure 2-2 and Figure 2-3. The intense spike of the PSD obtained by BJH at around 4 nm reflects an artefact (associated with the spontaneous evaporation of metastable pore liquid; Romero *et al.* 2012a). Nevertheless, the peak obtained by BJH at around 10 nm is more consistent with the one obtained by MIP.

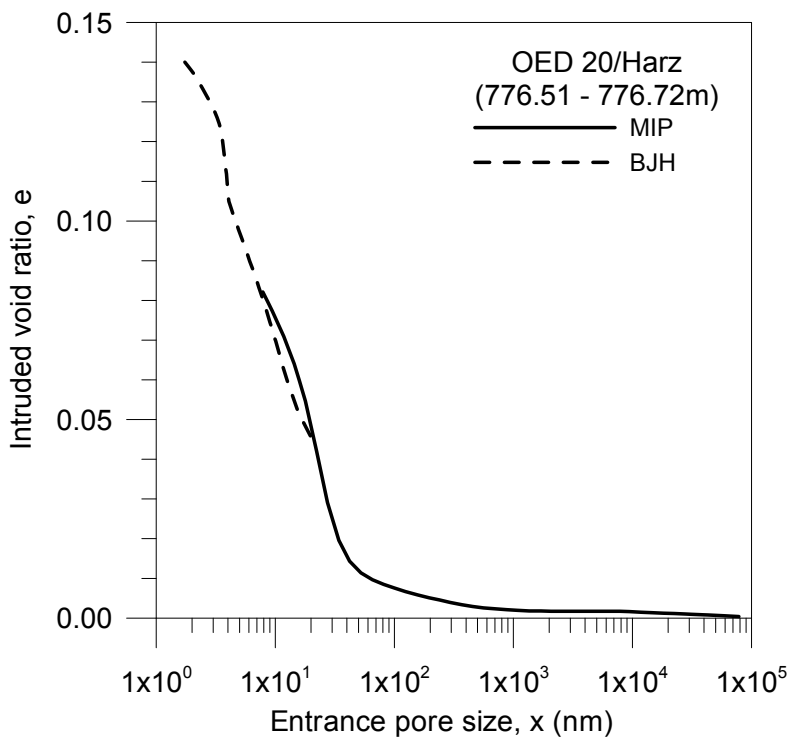


Fig. 2-2: Cumulated intruded void ratio (MIP and BJH). 'Brown Dogger' OED 20/Harz (776.51 - 776.72 m).

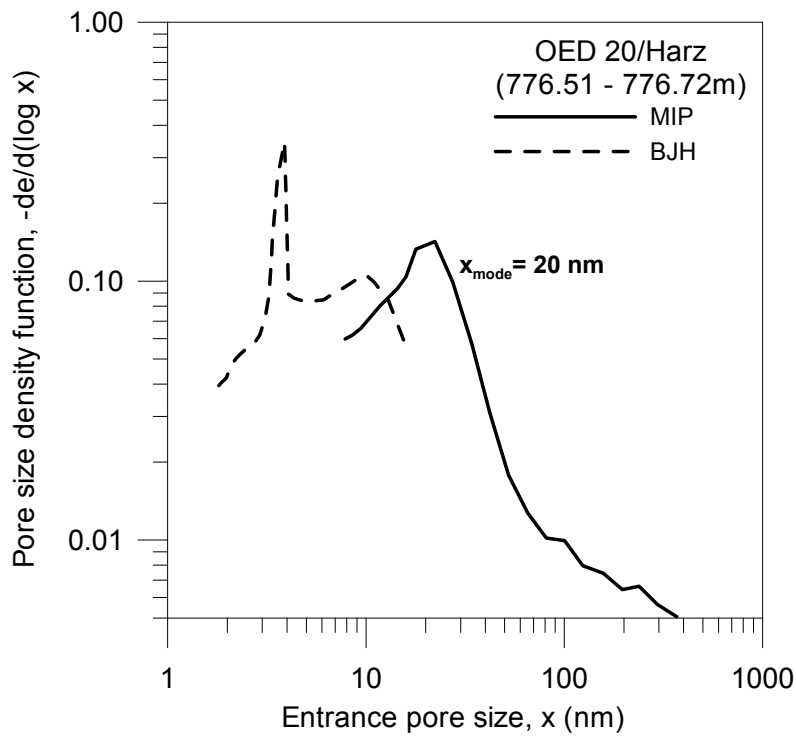


Fig. 2-3: PSD functions with dominant pore modes (MIP and BJH). 'Brown Dogger' OED 20/Harz (776.51 - 776.72 m).

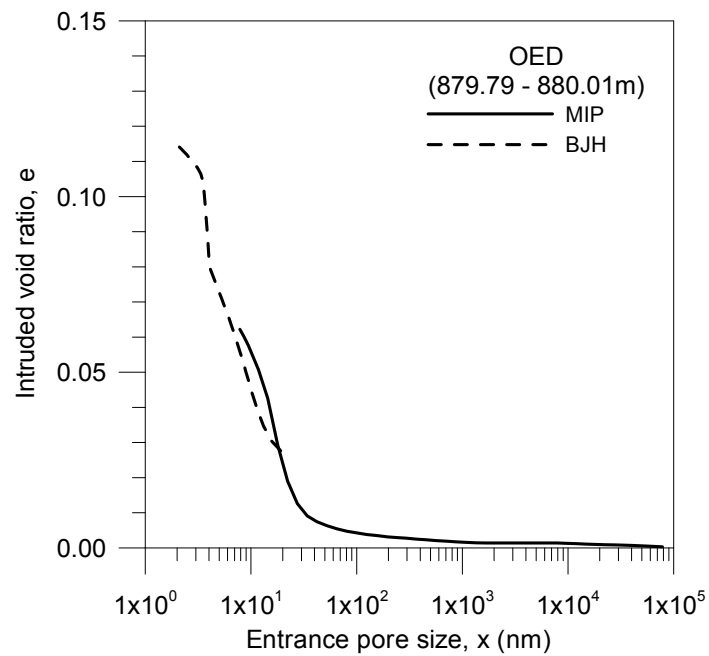


Fig. 2-4: Cumulated intruded void ratio (MIP and BJH). OPA OED (879.79 - 880.01 m).

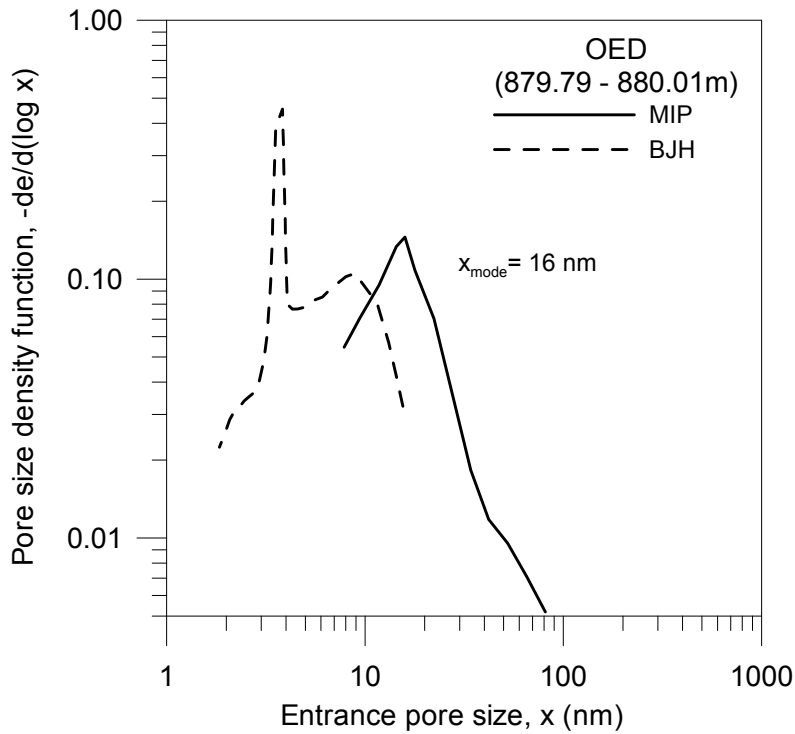


Fig. 2-5: PSD functions with dominant pore modes (MIP and BJH). OPA OED (879.79 - 880.01 m).

Figure 2-4 shows the equivalent cumulative intruded pore volume normalised by solid volume (intruded void ratio) plotted against the entrance pore size for the OPA sample (OED 879.79 - 880.01 m). The PSD function for this material is plotted in Figure 2-5. Again the intense spike of the PSD obtained by BJH at around 4 nm reflects an artefact (associated with the spontaneous evaporation of metastable pore liquid). The peak obtained by BJH, which is slightly lower than 10 nm, is also consistent with the smaller one obtained by MIP (16 nm for OPA with $\theta_{nw} = 147^\circ$). Dominant modes of the entrance pore size of the two tested materials have been included in Table 2-2.

A comparison between the cumulative and PSD functions of both materials is summarised in Figure 2-6 and Figure 2-7.

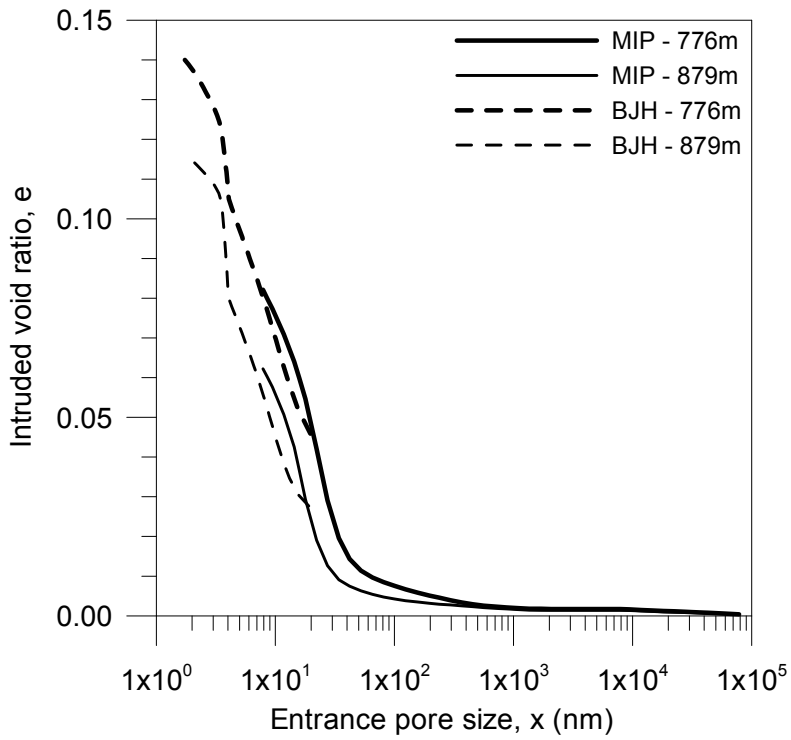


Fig. 2-6: Cumulated intruded void ratio (MIP and BJH). 'Brown Dogger' OED 20/Harz (776.51 - 776.72 m) and OPA OED (879.79 - 880.01 m).

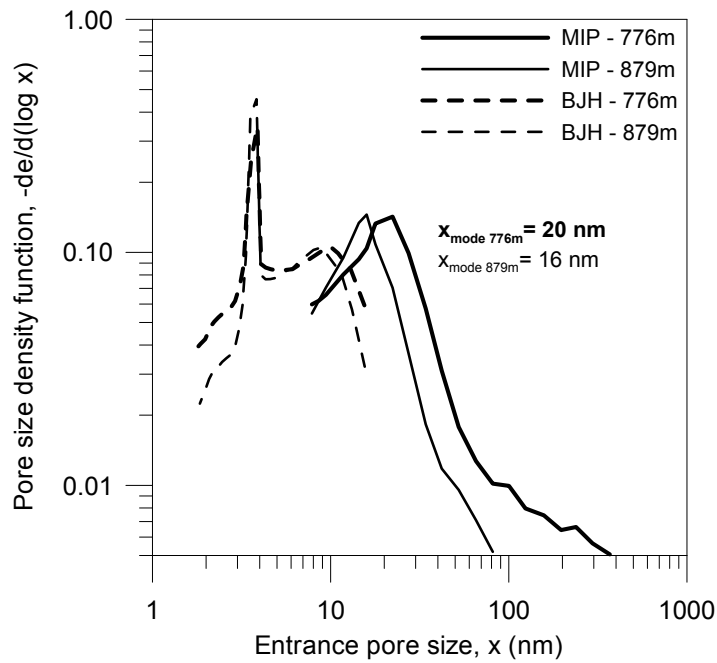


Fig. 2-7: PSD functions with dominant pore modes (MIP and BJH). 'Brown Dogger' OED 20/Harz (776.51 - 776.72 m) and OPA OED (879.79 - 880.01 m).

Figure 2-8 shows the comparison between the cumulative and PSD functions of a shallow OPA sample (approx. 300 m depth bg; BHA-8/1 in the shaly facies, MI-niche, Mont Terri Underground Laboratory) and the deep OPA sample. The left plot shows the cumulated intruded void ratio, whereas the right one shows the PSD functions with dominant pore modes. Dominant modes of the entrance pore size of OPA at two different depths have been included in Table 2-3.

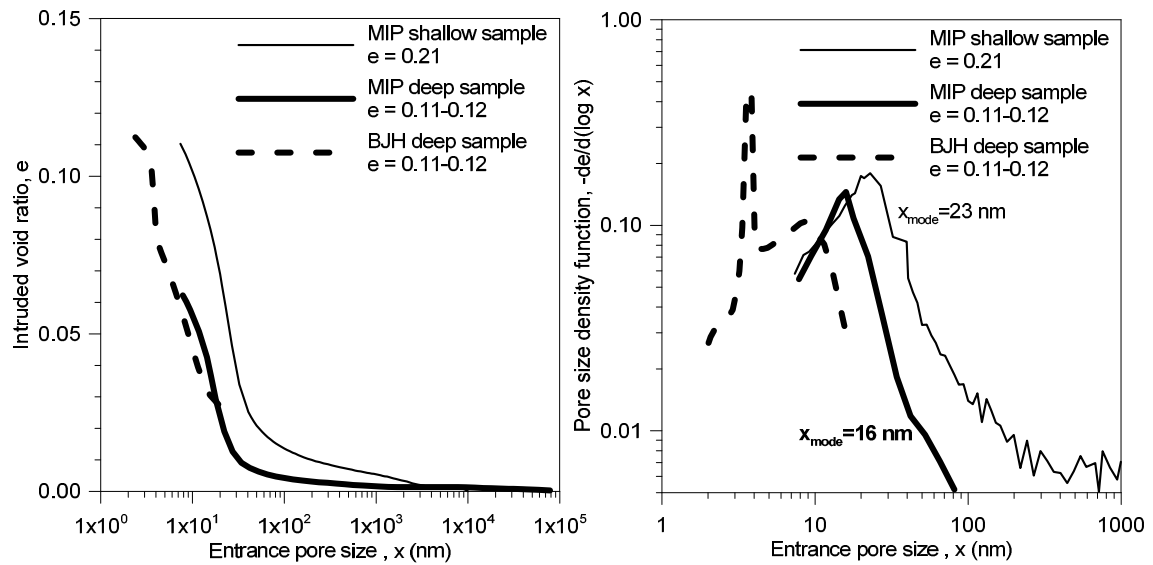


Fig. 2-8: Cumulated intruded void ratio (left) and PSD functions with dominant pore modes (right). Deep (879.9 m) and shallow (300 m) OPA samples.

2.3 Specimen preparation

The protocol followed to prepare the samples is summarised in Figure 2-9. A band saw was first used to pre-cut the PVC tube and core sample under dry conditions to a length around 100 mm. The sample was then sub-cored under dry conditions with a lathe to obtain a cross-section with 50 mm in diameter. Afterwards, cores were prepared to match a final height of 25 mm. Cores were then packed in plastic bags under vacuum.



Fig. 2-9: Steps followed to prepare specimen (50.0 mm in diameter and 25.4 mm high). (a) Pre-cutting a slice of the core sample under dry conditions with a band saw.

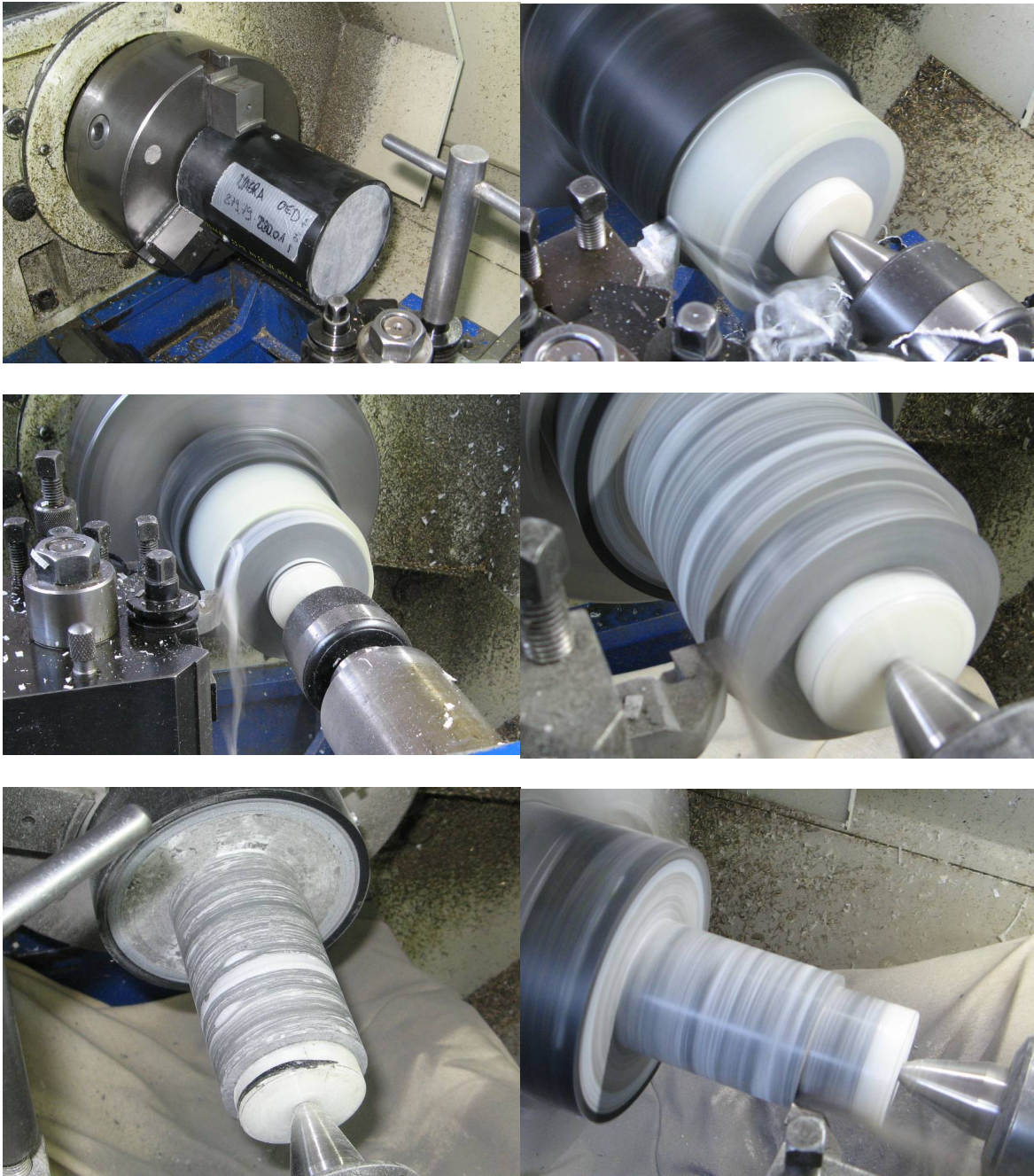
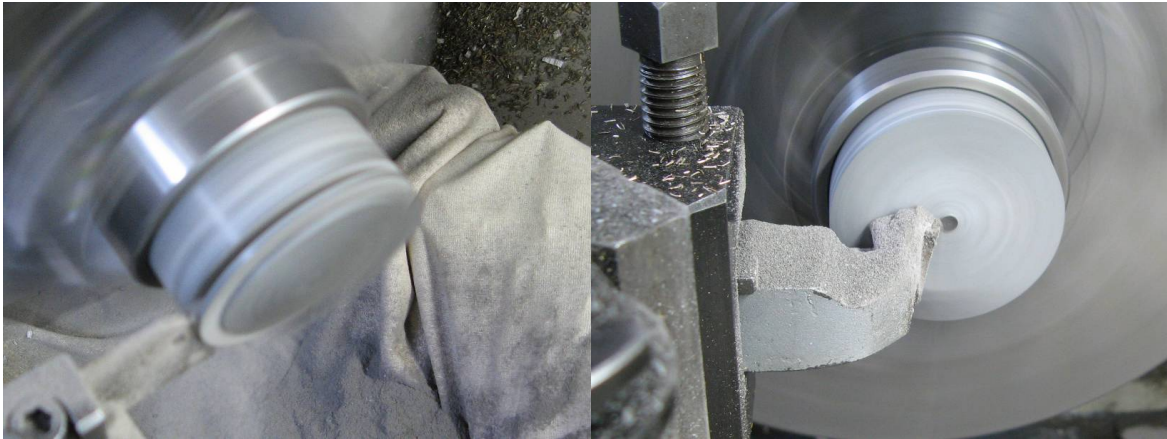
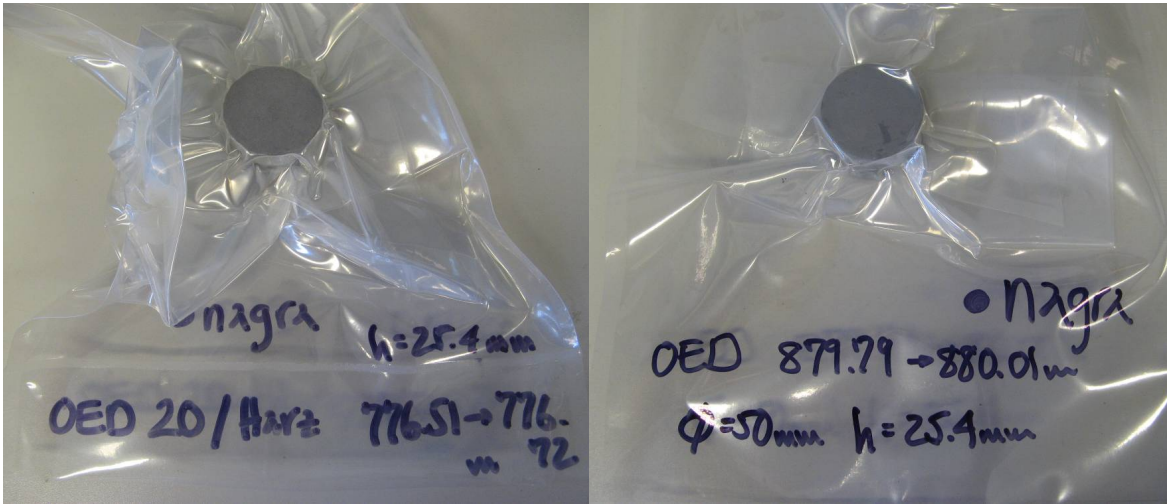


Fig. 2-9_{cont}: Steps followed to prepare specimen: (b) Preparing the circular cross-section (50.0 mm in diameter) with a lathe under dry conditions.



c) Finishing the preparation of the sample with a lathe to match 25.4 mm in height.



d) Samples sealed with two plastic bags under vacuum. Samples ready for testing.

Fig. 2-9_{cont}: Steps followed to prepare specimen (cont): finishing (c) and sealing of the samples.

2.4 Artificial pore water preparation

Approximately 3.5 kg of Artificial Pore Water (APW) were prepared following instructions given in paragraphs 4 and 5 of report AN 11-159 (NAGRA). After preparation, the APW solution was stirred for 5 days. Osmotic suction was measured using psychrometer readings (WP4 dewpoint potentiometer from Decagon Devices; Cardoso *et al.* 2007) and estimated from electrical conductivity measurements (Romero 1999). Table 2-4 summarises the main properties, where π is the measured or estimated osmotic suction, EC is the measured electrical conductivity and a_L is the estimated liquid activity (equivalent to the relative humidity RH of the air in contact with APW).

Tab. 2-4: Properties of Artificial Pore Water (APW).

| | π (MPa) | EC (mS/cm) | a_L (-) |
|-----|-------------|---------------|-----------------|
| APW | 1.04 – 1.10 | 19.30 – 19.42 | 0.9919 – 0.9923 |

2.5 Water retention curve

A dew point psychrometer (Cardoso *et al.* 2007) was used to obtain the water retention curves in the total suction range from 1 to 100 MPa. The specimens were dried in steps starting from the initial total suction, stored for one day for equalisation, weighed and the relative humidity of the air surrounding the soil measured. Pore size distribution results were also used to determine the relationship between matric suction and degree of saturation, as well as the air entry value corresponding to the dominant pore mode. The injection of non-wetting mercury was assumed to be equivalent to the ejection of water by the non-wetting front advance of air (drying branch) for the same diameter of pores being intruded. Fig. 2-10 and Fig. 2-11 show the estimated water retention curves based on MIP data together with psychrometric measurements for OED 20/Harz (776.51 - 776.72 m) and OED (879.79 - 880.01 m) samples, respectively. Fig. 2-12 shows the comparison of the results.

The air entry value AEV corresponding to the dominant pore mode detected from MIP data was determined using Laplace's equation. Table 2-2 and Table 2-3 report these AEVs for the different samples. Suction s and degree of saturation S_r data were fitted to van Genuchten's equation (1980)

$$S_r = \left[1 + (s / p_0)^n \right]^{-(1-1/n)} \quad (2)$$

Fitted parameters n and p_0 , the latter associated with the air entry value, are included in the figures, as well as in Table 2-2 and Table 2-3. A constant $n = 1.58$ has been considered for both samples. A slightly larger p_0 is consistently obtained for the deeper OED (879.79 - 880.01 m).

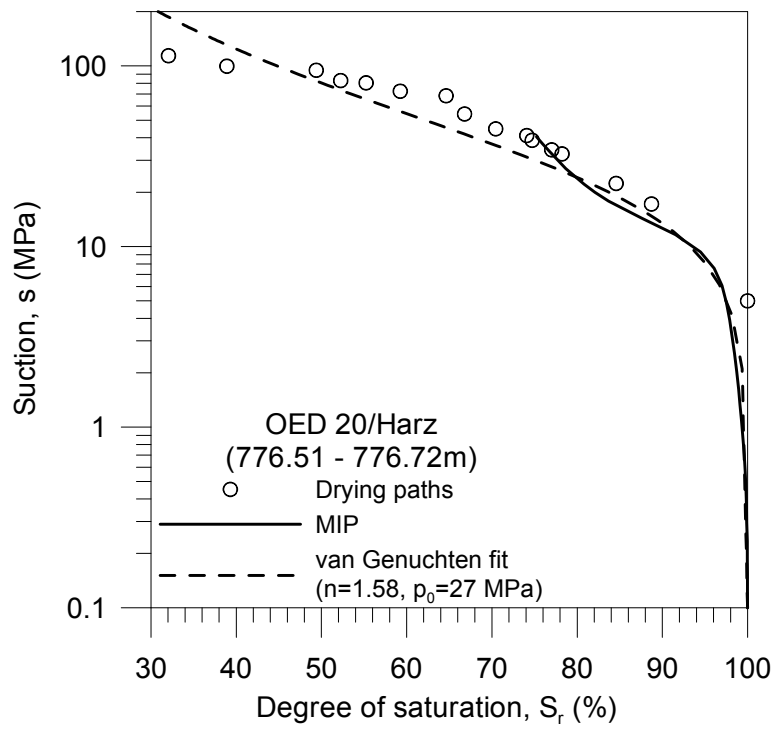


Fig. 2-10: Water retention curve. Sample OED 20/Harz (776.51 - 776.72 m).

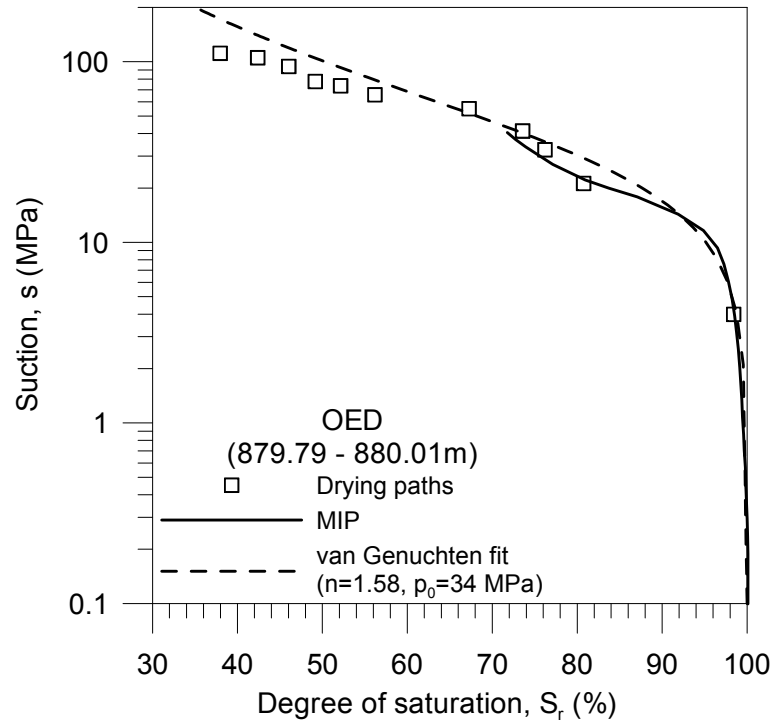


Fig. 2-11: Water retention curve. Sample OED (879.79 - 880.01 m).

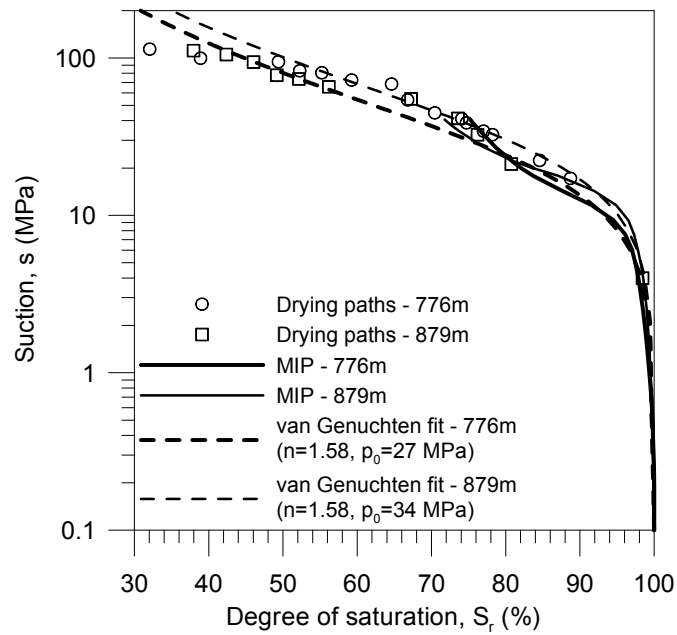


Fig. 2-12: Water retention curve. Comparison between OED 20/Harz (776.51 - 776.72 m) and OED (879.79 - 880.01 m) samples.

Figure 2-13 presents a comparison between the water retention curves of OPA samples at two different depths. The left plot shows the 'shallow sample' (approx. 300 m depth bg OPA; BHA-8/1 in the shaly facies, MI-niche), whereas the right plot presents the 'deep sample' (879.9 m depth bg OPA; Schlattingen borehole). A constant $n = 1.67$ has been considered to fit the van Genuchten curve. Again, a slightly larger p_0 is obtained for the deeper OED (879.79 - 880.01 m) sample.

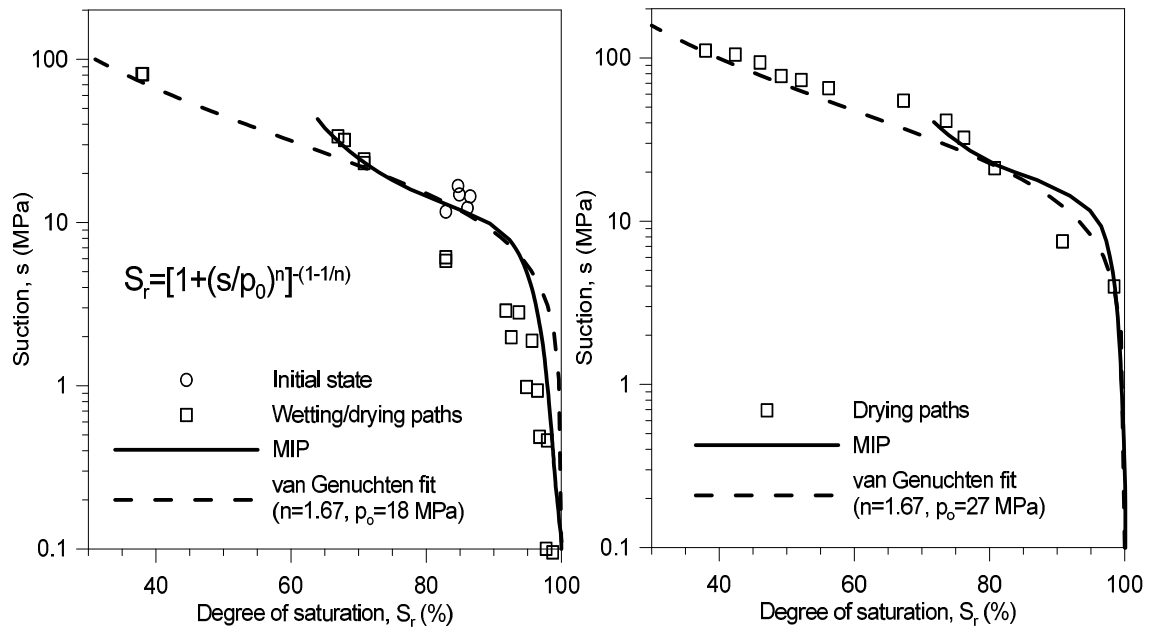


Fig. 2-13: Water retention curves of OPA samples. Left: 'Shallow sample' (BHA-8/1; approx. 300 m depth). Right: 'Deep sample' (OED 879.9 m depth).

2.6 Equipment, experimental set-up and test procedure

Equipment and experimental set-up

An instrumented high-pressure triaxial cell was used, which was specifically designed to apply isotropic/anisotropic stress states up to a maximum of 40 MPa, while injecting air at controlled volume rate (Pineda *et al.* submitted). Figure 2-14 shows a picture of the triaxial cell jointly with the test set-up. The axial deformation of low-height specimens –confined by several neoprene membranes and aluminium foils– is registered with an external linear variable differential transformer (LVDT in the figure). Each cap of the triaxial cell has inlet and outlet lines, prepared for gas and liquid connections. The equipment uses five automatic pressure / volume controllers (PVC in the figure), one to apply confining stress with water pressure up to 64 MPa, two for gas (injection at upstream point and extraction at downstream point), and two for APW (water injection at upstream point up to 32 MPa), which can be used in combination (for example, air injection and water pressure at downstream, which is the setup used in the present investigation). The gas injection PVC (Wille Geotechnik, Germany) has a maximum range of 20 MPa (maximum volume 500 mL), and is able to control volume rates between 10^{-4} mL/min and 100 mL/min (volume resolution $< 5 \text{ mm}^3$). The 2 MPa PVC controllers (GDS Instruments Ltd., United Kingdom) for air and water at downstream present a volumetric resolution of 1 mm^3 (pressure resolution 1 kPa). Figure 2-15 shows a cross-section of the high-pressure triaxial cell.

Figure 2-16 presents a scheme of the triaxial cell and the test set-up. Each of the different circuits was independently checked for system leakage at high pressures. The air pressure was increased to 18 MPa and then verified that it was maintained over time under closed system conditions (valve closed).

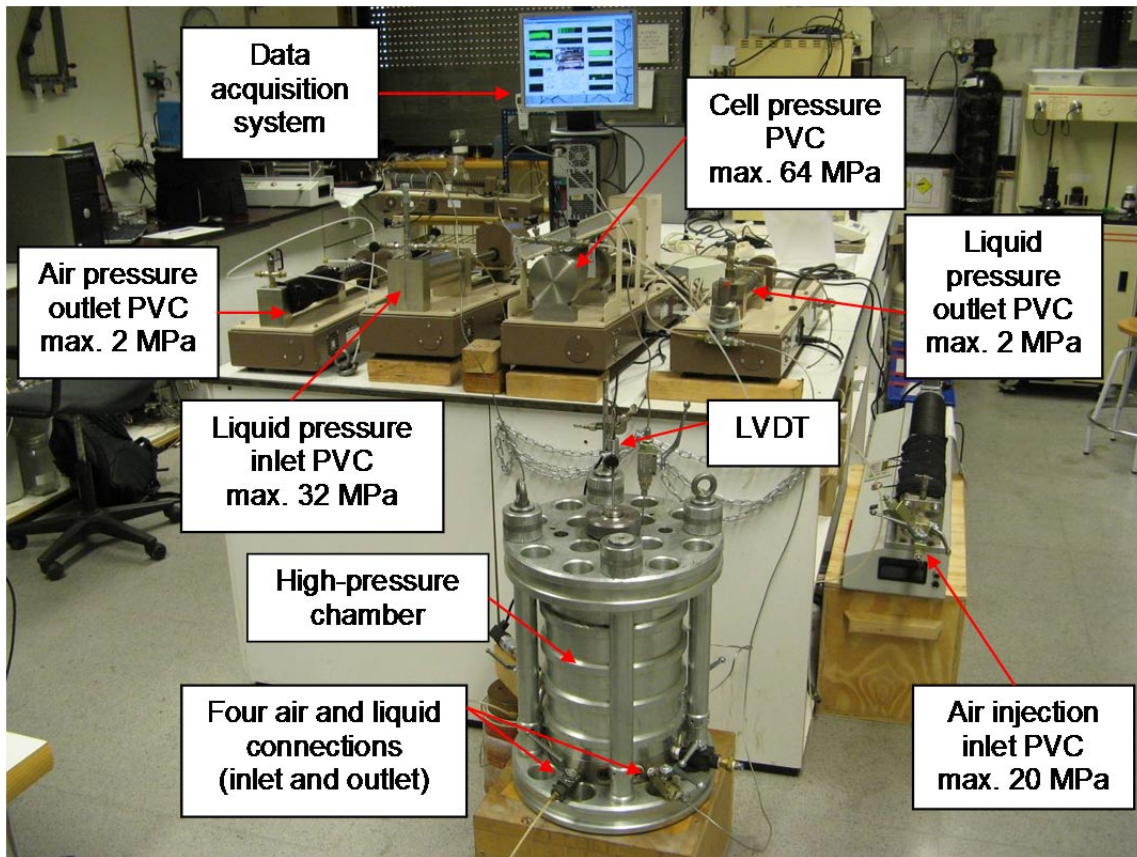


Fig. 2-14: Overview of the instrumented high-pressure triaxial cell.

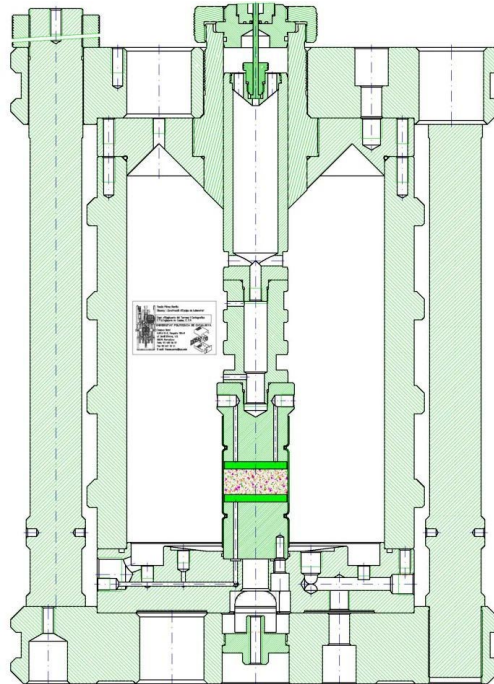


Fig. 2-15: Cross-section of the high-pressure triaxial cell.

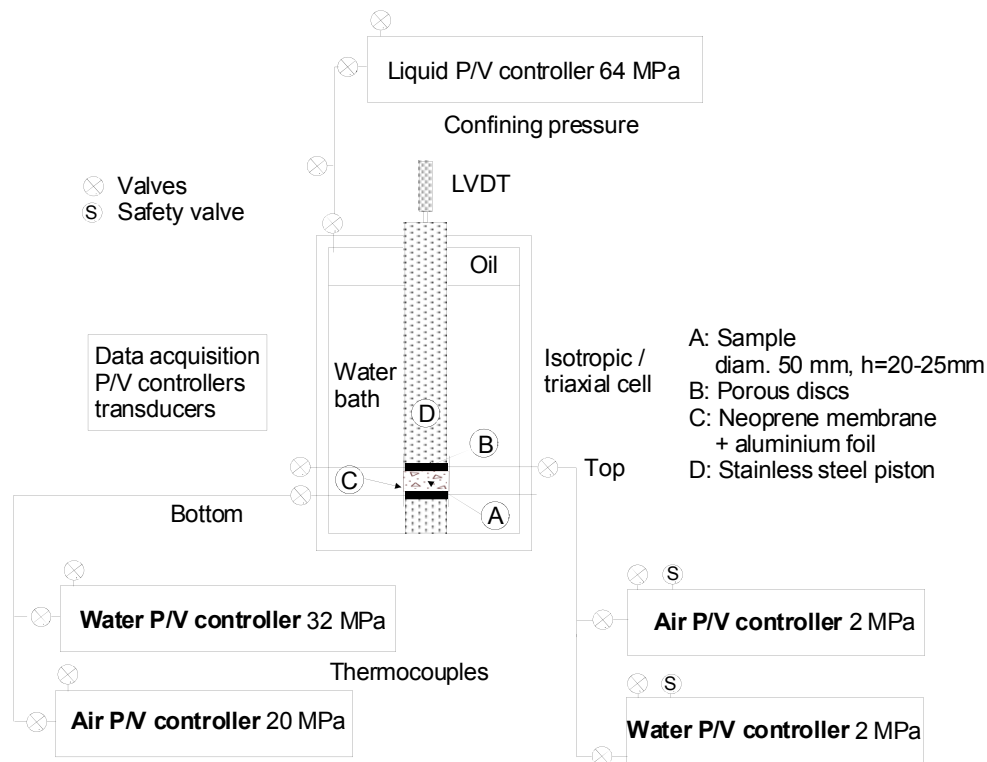


Fig. 2-16: Scheme of the air injection and water permeability setup with high-pressure triaxial cell and four pressure/volume controllers (two for air and two for water).

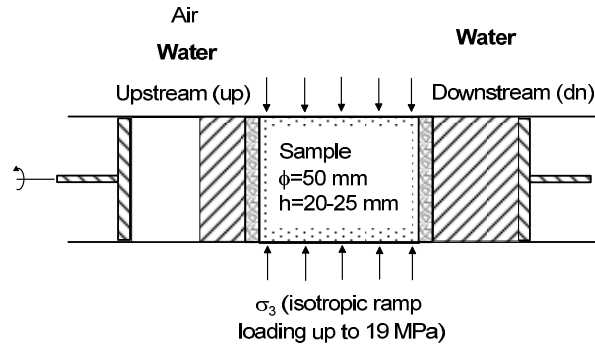
Experimental study performed

Before the air injection tests, saturation of the samples (flow orthogonal to bedding) was ensured and water permeability measured using different hydraulic gradients at different isotropic confining stresses (10, 11.75, 13.25 and 15 MPa). Figure 2-17 displays a scheme of this test *A*, in which upstream / downstream volume changes and axial deformation are recorded during these hydraulic tests. This information allows approximately plotting water permeability as a function of void ratio in these low-height samples (25.4 mm in height). Controlled-gradient conditions were maintained for around two/three weeks to ensure approximately equivalent inflow and outflow liquid volume rates (stationary flow conditions).

For the air injection tests (test *B* in Figure 2-17), the upstream water line was rapidly drained to inject air pressure at 0.5 MPa and the recovery system maintained with water at 0.5 MPa to better ensure sample saturation. The sample was let to equalise at an initial pore water pressure of 0.5 MPa and at the target total isotropic stress (15 or 19 MPa). Fast air injection started under controlled volume rates (100 mL/min) from an initial value of 3 MPa. After reaching maximum air pressure (1 MPa lower than the confining stress: 14 or 18 MPa), the upstream piston was stopped and air pressure was let to decay at constant volume. Fitting the constant mass system for different injection periods allowed estimating the initial injection volume of air (injection piston and air lines). Pressure deviations from the perfect gas law for a constant mass system in the injection point allowed estimating the injected mass of air and mass inflow rates into the sample. Information on outflow rates was recorded and used to define the breakthrough pressures.

Specimen mounting

Samples 50.0 mm in diameter and 25.4 mm high were installed in the triaxial cell using three 1-mm thick neoprene membranes. Aluminium foils stuck with silicone grease were placed between membranes. Two o-rings and a metallic clamp were used at each end. Figure 2-18 shows the different steps followed during sample installation.

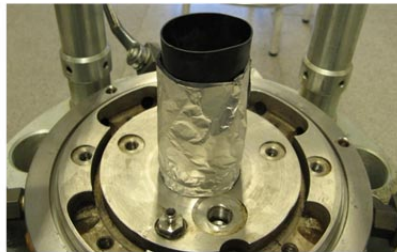


- A** Water permeability (starting from saturated state):
 $P_{up} = \text{const.}_1$ (water); $P_{dn} = \text{const.}_2$ (water)
 dV/dt (upstream and downstream volumes)
- B** Pressure pulse / decay air test:
 Sudden P_{up} (air); then $V_{up} = \text{const.}_1$ (air)
 $P_{dn} = \text{const.}_2$ (water) (initial condition)
 time evolution of P_{up} and V_{dn}

Fig. 2-17: Type of tests followed during controlled-gradient water permeability tests and fast air injection tests followed by recovery period at constant volume.



Sample sealed with plastic under vacuum (ϕ 50mm; h25mm)



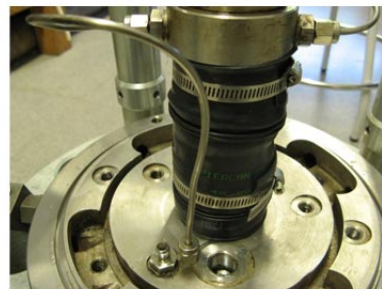
Sample confined by Neoprene membrane and aluminium foil



Installation of a second Neoprene membrane (aluminium foil is between the membranes)



Installation of a third Neoprene membrane



Cap installation and inlet/outlet upper connections

Fig. 2-18: Steps followed during sample installation in the triaxial cell.

Test protocols followed

The different stages followed along the experimental program are summarised below:

- Isotropic loading from 0.1 to 10 MPa at constant water content. A constant stress rate of 30 kPa/min was used followed by an equalisation period of 1 day.
- Application of water pressures at upstream (bottom cap) and downstream (top cap) points to induce flow of water through the sample. Upstream pressure was increased from 0 to 2 MPa and downstream pressure from 0 and 0.5 MPa (this top cap pressure was maintained constant along the different stages of the test). Axial deformation was monitored along this hydraulic process. Water permeability was measured under steady state conditions. This stage lasted a minimum of two weeks.
- Isotropic loading from 10 to 11.75 MPa and simultaneous increase of the upstream pressure from 2 to 5.5 MPa. Axial deformation was monitored along this hydro-mechanical process. Water permeability was measured under steady state conditions. This stage lasted a minimum of two weeks.
- Isotropic loading from 11.75 to 13.25 MPa and simultaneous increase of the upstream pressure from 5.5 to 8.5 MPa. Axial deformation was monitored along this hydro-mechanical process. Water permeability was measured under steady state conditions. This stage lasted a minimum of two weeks.
- Isotropic loading from 13.25 to 15 MPa. The upstream water pressure was maintained constant at 8.5 MPa. Axial deformation was monitored along this mechanical process. Water permeability was measured under steady state conditions. This stage lasted a minimum of two weeks.
- Decrease of upstream water pressure from 8.5 to 0.5 MPa at constant isotropic stress of 15 MPa. Axial deformation was monitored along this hydraulic process. This stage lasted a minimum of one week to allow for pore pressure equalisation.
- Water pressure in the upstream vessel was reduced to atmospheric conditions to allow for its fast replacement by air. Air pressure at upstream point was rapidly increased from atmospheric conditions to 3 MPa. Isotropic stress was kept constant at 15 MPa.
- Fast air injection test from 3 to 14 MPa at constant flow rate of 100 mL/min (constant isotropic stress of 15 MPa), followed by a shut-in and recovery phase at constant volume. Measurement of the evolution of upstream and downstream pressures, as well as outflow volume and sample axial deformation, during the injection and dissipation stages. This stage lasted a minimum of three weeks.
- Air pressure in the upstream vessel was reduced to atmospheric conditions to allow for its fast replacement by water. Upstream water pressure was then increased to 0.5 MPa to allow for sample re-saturation and water pore pressure equalisation. This stage was maintained for one / two weeks.
- Isotropic stress increase from 15 to 19 MPa at constant pore water pressure of 0.5 MPa (upstream and downstream water pressures were kept at 0.5 MPa). Axial deformation was monitored along this mechanical process. This stage lasted one / two weeks to allow for pore pressure equalisation.
- Water pressure in the upstream vessel was then reduced to atmospheric conditions to allow for its fast replacement by air. Isotropic stress was kept constant at 19 MPa. Air pressure at upstream point was rapidly increased from atmospheric conditions to 3 MPa.

- Fast air injection test from 3 to 18 MPa at constant flow rate of 100 mL/min (constant isotropic stress of 19 MPa), followed by a shut-in and recovery phase at constant volume. Measurement of the evolution of upstream and downstream pressures, as well as outflow volume and sample axial deformation, during the injection and dissipation stages. This stage lasted a minimum of three weeks.
- Upstream air pressure was reduced to 0.5 MPa. Isotropic stress was then decreased from 19 to 0.5 MPa. This stage lasted 1 day.
- Isotropic unloading from 0.5 MPa to 0. Simultaneously, both upstream and downstream pressures were reduced from 0.5 MPa to 0. There was no post-mortem sample characterisation after finishing the air tests.

3 Test Results

3.1 Compressibility on mean stress and pore pressure changes

Figure 3-1 shows the axial deformation on isotropic loading from 0.1 to 10 MPa at constant water content for the two tested materials (OED 20/Harz 'Brown Dogger' at 776.51 - 776.72 m, and deep OED Opalinus Clay at 879.79 - 880.01 m). If no important radial straining during this process on the low-height specimen is assumed (friction at the top and bottom boundaries are considered to affect this lateral deformation), then the approximate bulk modulus can be estimated as $K = \delta(p - u_w) / \delta \varepsilon_p$, where p is the mean total stress, u_w the pore water pressure and ε_p the volumetric strain (equivalent to the axial component since radial straining was considered negligible). The bulk moduli of both materials are reported in Table 3-1.

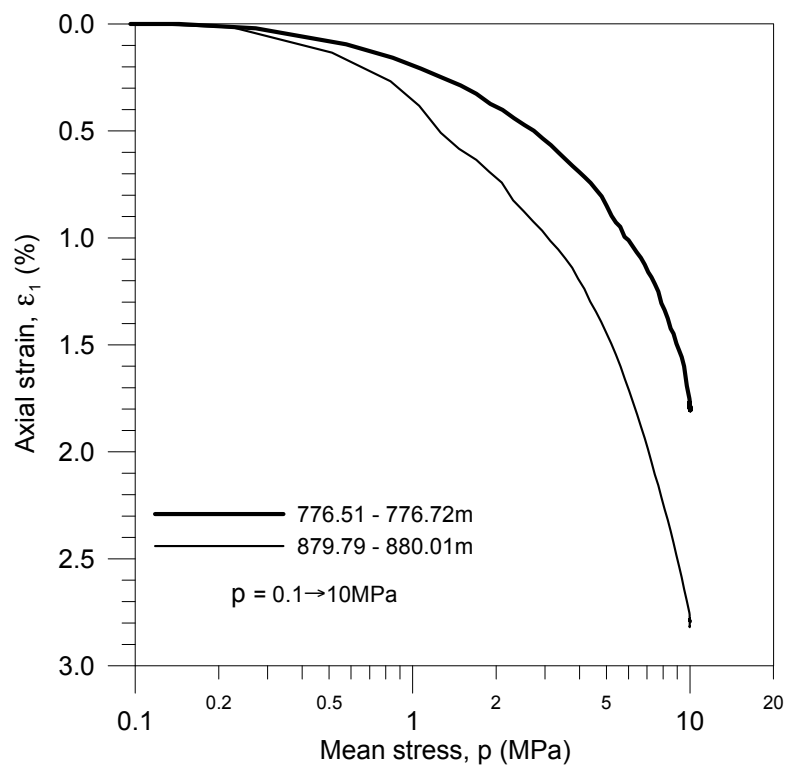


Fig. 3-1: Compression curves during isotropic loading from 0.1 to 10 MPa at constant water content for OED 20/Harz 'Brown Dogger' at 776.51 - 776.72 m, and deep OED Opalinus Clay at 879.79 - 880.01 m.

Swelling strains (negative strains correspond to swelling) during water pressure application (flooding) at constant $p = 10$ MPa for OED 20/Harz 'Brown Dogger' at 776.51 - 776.72 m, and deep OED Opalinus Clay at 879.79 - 880.01 m, are shown in Figure 3-2. This swelling is associated with effective stress reduction (pore water pressure increases from a low value – probably at an initial value near atmospheric conditions– to a value of around 1.25 MPa – average value of pressures applied at the boundaries–). With this assumption ($\delta u_w \approx 1.25$ MPa), the estimated bulk moduli reported in Table 3-1 are not different to those obtained for the previous loading stage at constant water content. These results (Figure 3-1 and Figure 3-2) suggest that OED 20/Harz 'Brown Dogger' is slightly stiffer than deep OED Opalinus Clay.

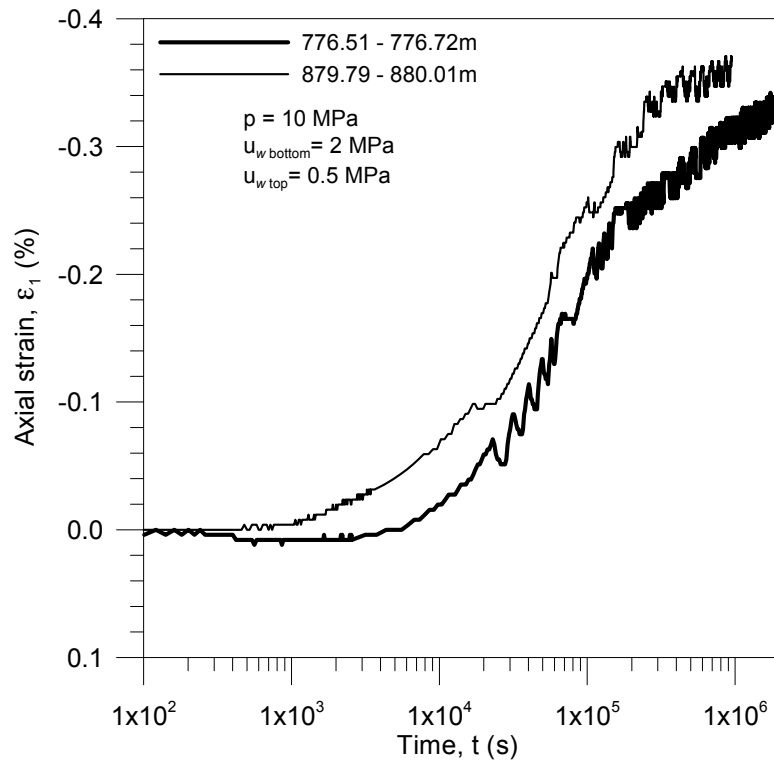


Fig. 3-2: Swelling (negative strains correspond to swelling) during water pressure application (flooding) at constant $p = 10$ MPa for OED 20/Harz 'Brown Dogger' at 776.51 - 776.72 m, and deep OED Opalinus Clay at 879.79 - 880.01 m.

The volume change curves for the different stages applied on both materials for the water permeability determinations at different stress states (different p and different u_w) are reported in Figure 3-3 to Figure 3-6.

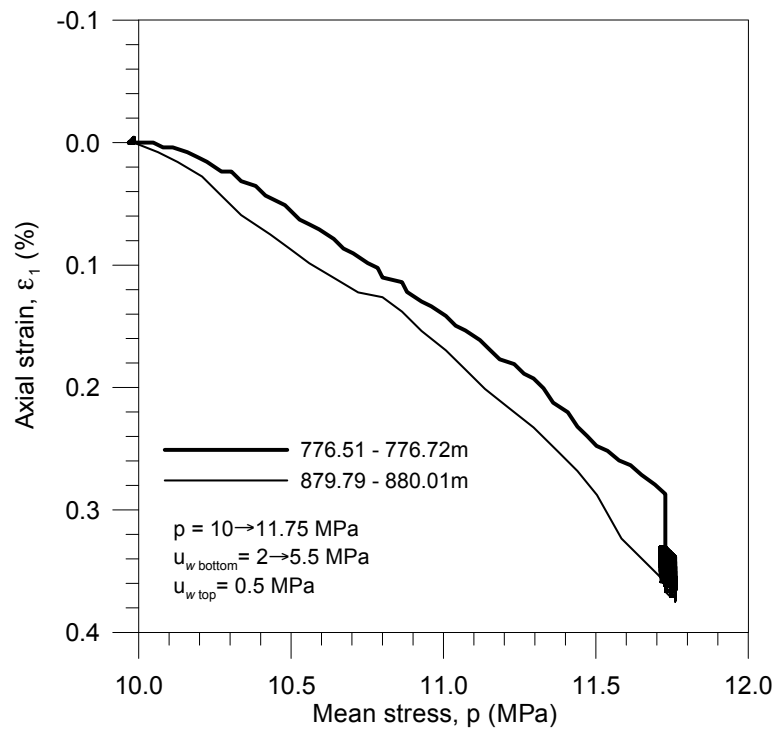


Fig. 3-3: Axial strain evolution during p change from 10 to 11.75 MPa and u_w change (bottom cap) from 2 to 5.5 MPa. OED 20/Harz 'Brown Dogger' at 776.51 - 776.72 m, and deep OED Opalinus Clay at 879.79 - 880.01 m.

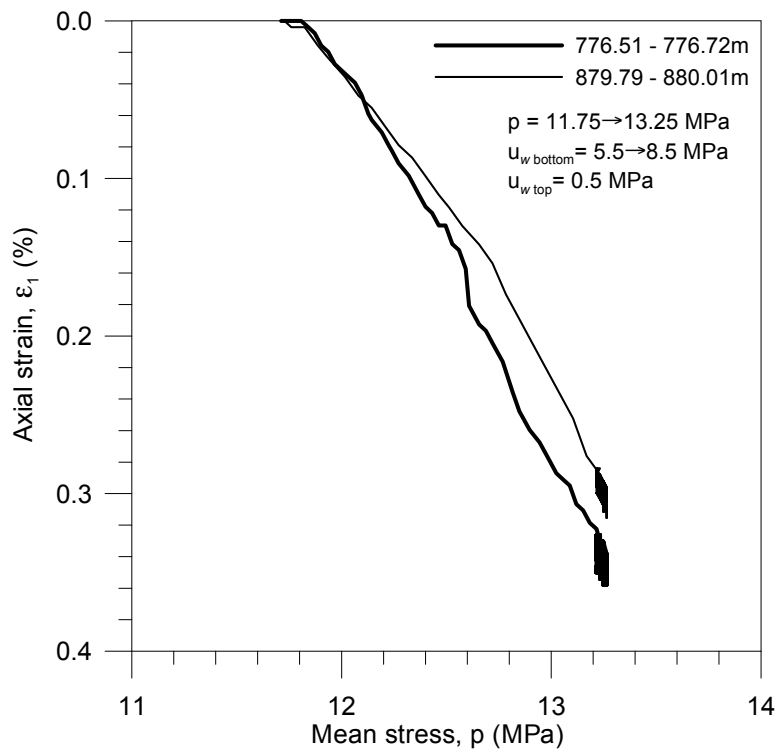


Fig. 3-4: Axial strain evolution during p change from 11.75 to 13.25 MPa and u_w change (bottom cap) from 5.5 to 8.5 MPa. OED 20/Harz 'Brown Dogger' at 776.51 - 776.72 m, and deep OED Opalinus Clay at 879.79 - 880.01 m.

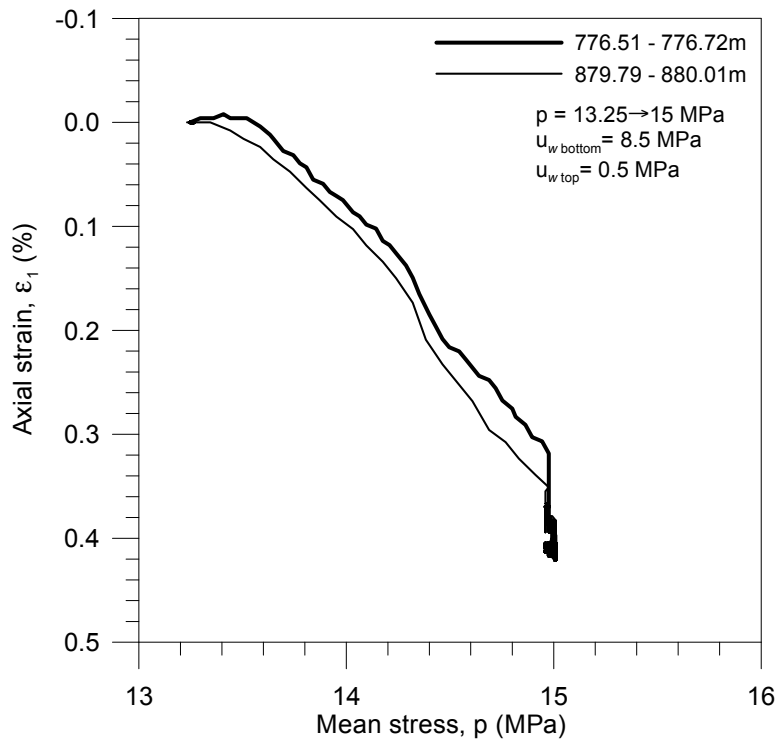


Fig. 3-5: Axial strain evolution during p change from 13.25 to 15 MPa and at constant $u_w = 8.5$ MPa (bottom cap). OED 20/Harz 'Brown Dogger' at 776.51 - 776.72 m, and deep OED Opalinus Clay at 879.79 - 880.01 m.

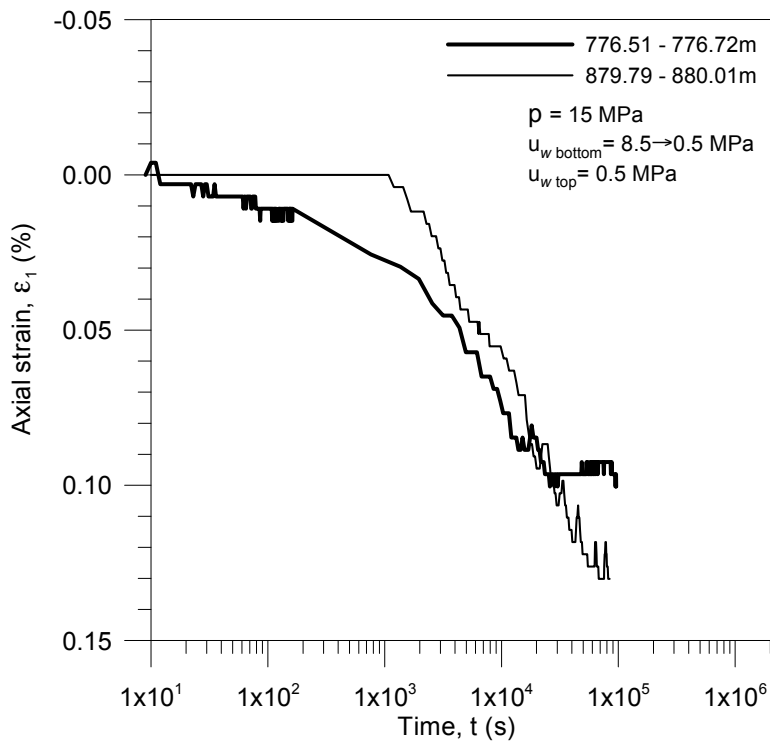


Fig. 3-6: Axial strain evolution at constant $p = 15$ MPa and u_w change (bottom cap) from 8.5 to 0.5 MPa. OED 20/Harz 'Brown Dogger' at 776.51 - 776.72 m, and deep OED Opalinus Clay at 879.79 - 880.01 m.

Table 3-1 summarises the different loading / unloading stages followed on both materials for the water permeability determinations at different stress states (different p and different u_w). The table includes the axial strain undergone and the final void ratio attained during each stage. Final void ratios are estimated assuming that no important radial straining occurred during the different stages (friction at the top and bottom boundaries are considered to affect this lateral deformation of the low-height specimen):

$$e \approx e_o - \varepsilon_1(1 + e_o)$$

where ε_1 : axial strain

and e_o : initial void ratio

(3)

Tab. 3-1: Different loading/unloading stages followed on both materials for the water permeability determinations.

| | OED 20/Harz 'Brown Dogger' (776.51 - 776.72 m) | | OED Opalinus Clay (879.79 - 880.01 m) | |
|--|--|-----------------------|--|-----------------------|
| Stage | Axial strain (%) (bulk modulus) | Approx. void ratio | Axial strain (%) (bulk modulus) | Approx. void ratio |
| Initial | --- | $e_o = 0.130$ | --- | $e_o = 0.109$ |
| $p = 0.1$ to 10 MPa at constant water content | 1.805 ($K = 548$ MPa) | 0.110 | 2.819 ($K = 351$ MPa) | 0.078 |
| $p = 10$ MPa; $u_{wbottom} = 2$ MPa; $u_{wtop} = 0.5$ MPa | -0.342 ($K \approx 365$ MPa, assuming $\delta u_w \approx 1.25$ MPa) | 0.113 | -0.371 ($K \approx 337$ MPa, assuming $\delta u_w \approx 1.25$ MPa) | 0.082 |
| $p = 10$ to 11.75 MPa; $u_{wbottom} = 2$ to 5.5 MPa; $u_{wtop} = 0.5$ MPa | 0.366 | 0.109 | 0.375 | 0.078 |
| $p = 11.75$ to 13.25 MPa; $u_{wbottom} = 5.5$ to 8.5 MPa; $u_{wtop} = 0.5$ MPa | 0.358 | 0.105 | 0.315 | 0.074 |
| $p = 13.25$ to 15 MPa; $u_{wbottom} = 8.5$ MPa; $u_{wtop} = 0.5$ MPa | 0.421 ($K = 416$ MPa) | 0.101 | 0.402 ($K = 435$ MPa) | 0.070 |
| $p = 15$ MPa; $u_{wbottom} = 8.5$ to 0.5 MPa; $u_{wtop} = 0.5$ MPa | 0.100 | 0.099 | 0.130 | 0.068 |

3.2 Water permeability results - time evolution of water volume change

OED 20/Harz 'Brown Dogger' (776.51 - 776.72 m) sample

Figure 3-7 to Figure 3-10 present the time evolution of water volume inflow and outflow (V_w) during the four stages for water permeability determination reported in Table 3-1. Some small leakage problems were detected in the outflow pressure / volume controller, particularly during the last two stages.

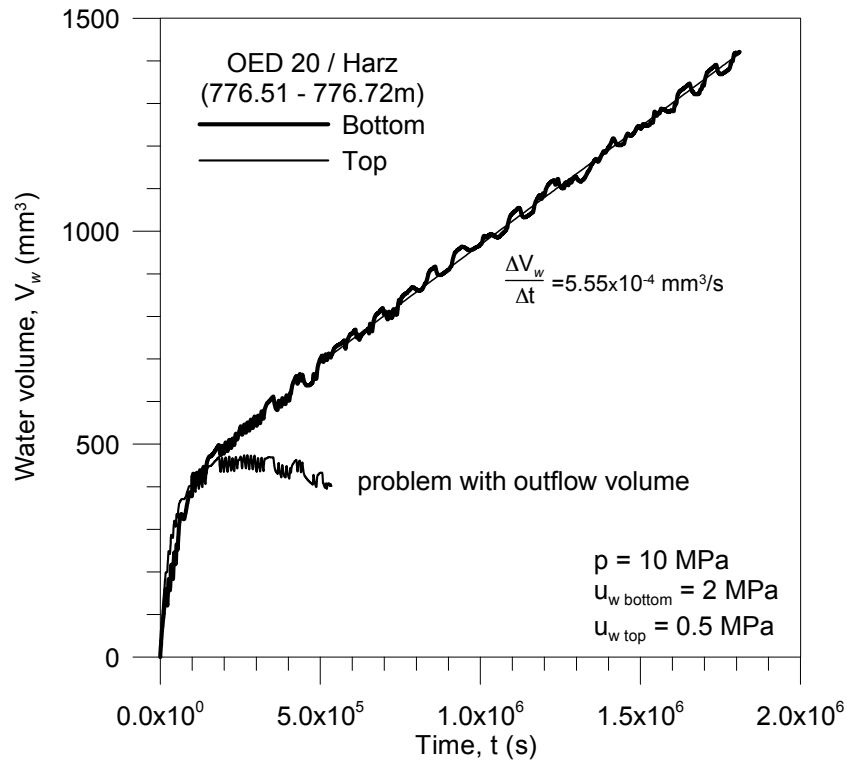


Fig. 3-7: Time evolution of water inflow / outflow volumes. Stage at $p = 10 \text{ MPa}$; $u_{w \text{ bottom}} = 2 \text{ MPa}$; $u_{w \text{ top}} = 0.5 \text{ MPa}$. OED 20/Harz 'Brown Dogger' sample.

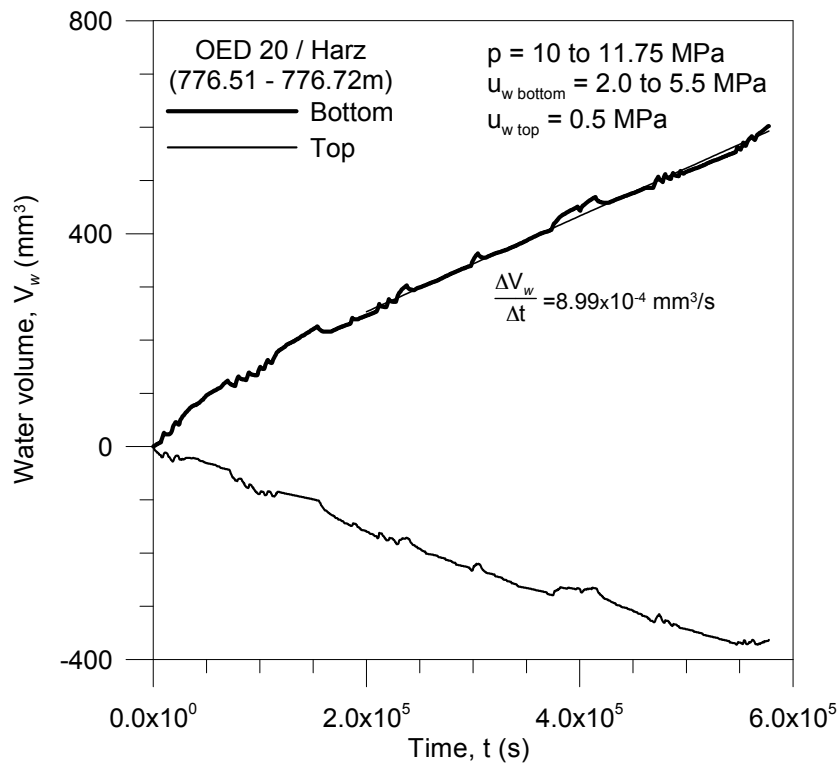


Fig. 3-8: Time evolution of water inflow / outflow volumes. Stage at $p = 11.75$ MPa; $u_{w\text{bottom}} = 5.5$ MPa; $u_{w\text{top}} = 0.5$ MPa. OED 20/Harz 'Brown Dogger' sample.

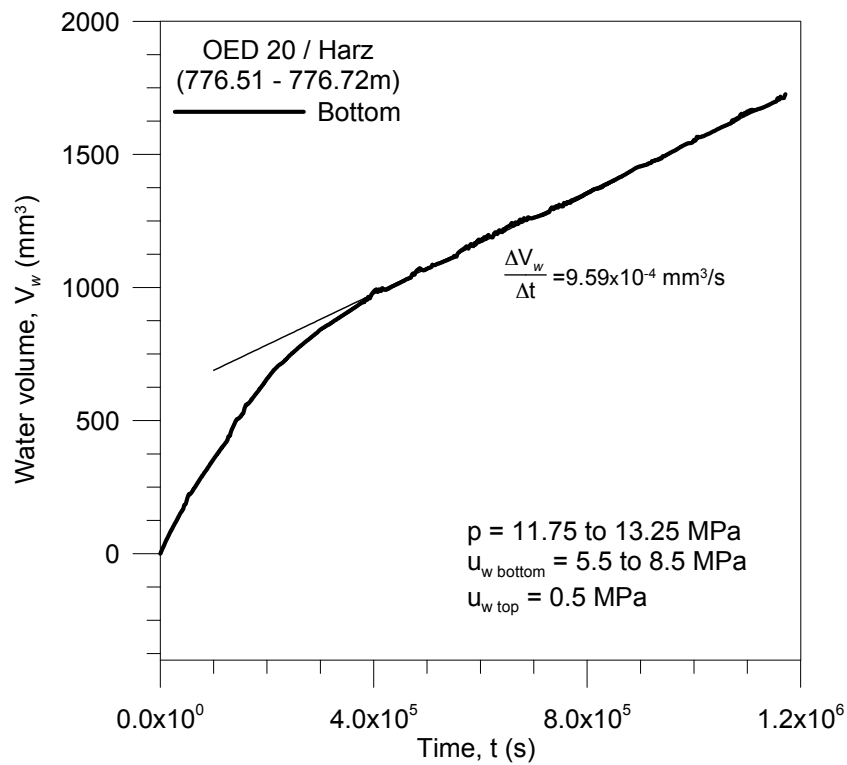


Fig. 3-9: Time evolution of water inflow volume. Stage at $p = 13.25$ MPa; $u_{w\text{bottom}} = 8.5$ MPa; $u_{w\text{top}} = 0.5$ MPa. OED 20/Harz 'Brown Dogger' sample.

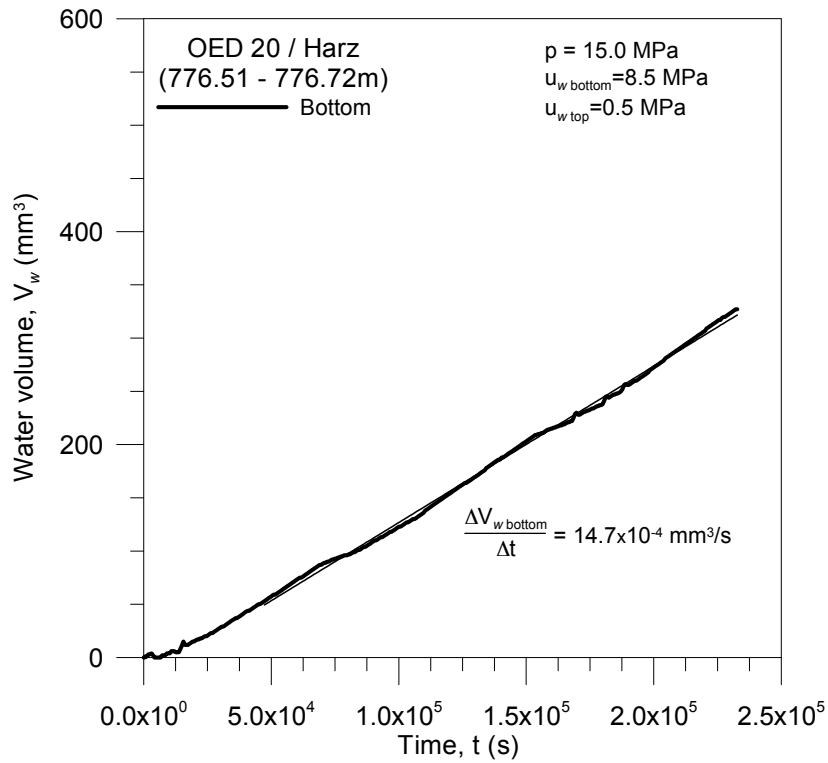


Fig. 3-10: Time evolution of water inflow volume. Stage at $p = 15.0 \text{ MPa}$; $u_{w \text{ bottom}} = 8.5 \text{ MPa}$; $u_{w \text{ top}} = 0.5 \text{ MPa}$. OED 20/Harz 'Brown Dogger' sample.

Figure 3-11 to Figure 3-14 show the time evolutions in terms of $\Delta V_w / (A i \Delta t)$, where A is the sample cross-section, i the hydraulic gradient applied (Table 3-2), V_w the water volume flowing through the sample, and t the elapsed time. Changes in volume and time are referred to a fixed initial value under steady state conditions (under steady state conditions, $\Delta V_w / (A i \Delta t)$ corresponds to water permeability k_w shown in the figures and summarised in Table 3-2).

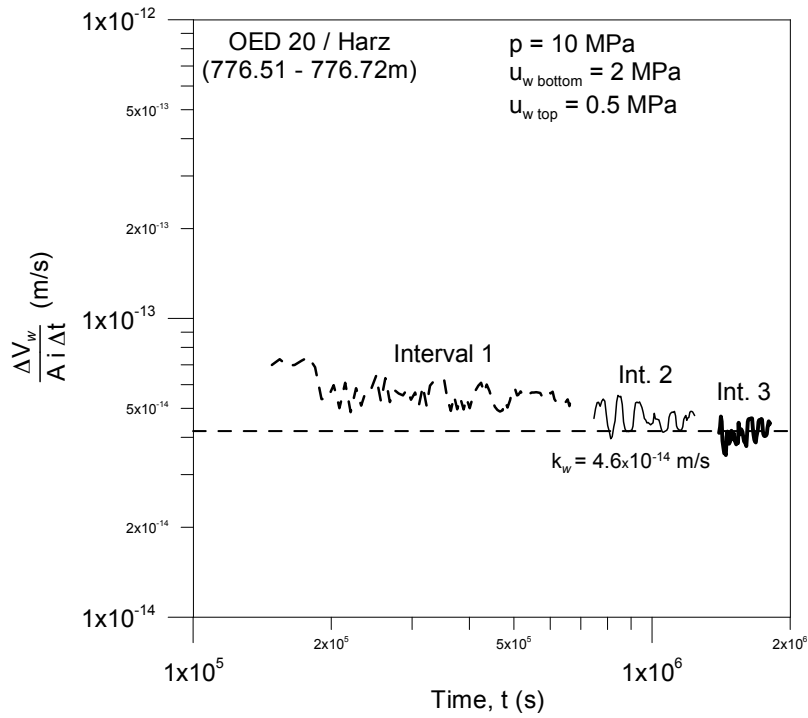


Fig. 3-11: Time evolution of $\Delta V_w / (A_i \Delta t)$ (three intervals have been considered under steady state conditions). Stage at $p = 10 \text{ MPa}$; $u_{w \text{ bottom}} = 2 \text{ MPa}$; $u_{w \text{ top}} = 0.5 \text{ MPa}$. OED 20/Harz 'Brown Dogger' sample.

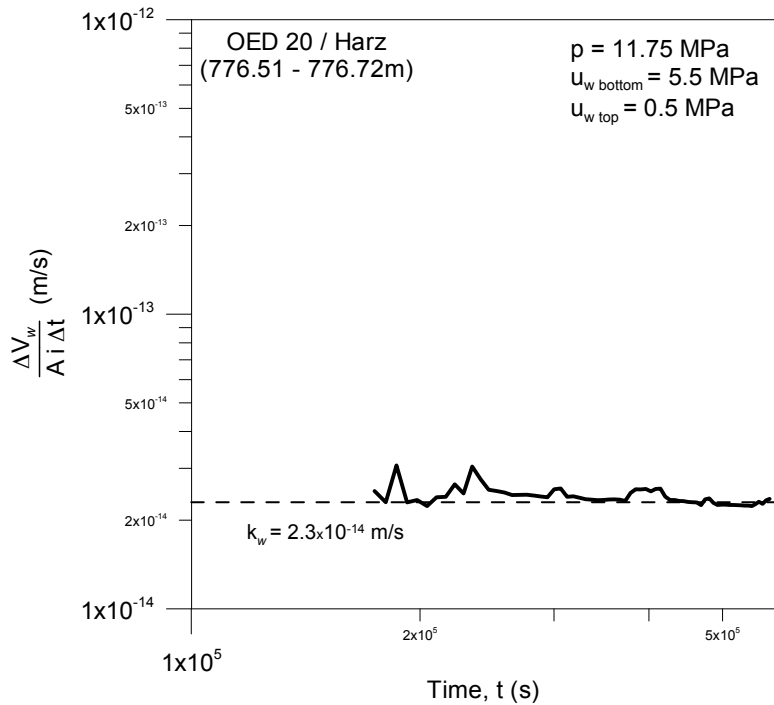


Fig. 3-12: Time evolution of $\Delta V_w / (A_i \Delta t)$ under steady state conditions. Stage at $p = 11.75 \text{ MPa}$; $u_{w \text{ bottom}} = 5.5 \text{ MPa}$; $u_{w \text{ top}} = 0.5 \text{ MPa}$. OED 20/Harz 'Brown Dogger' sample.

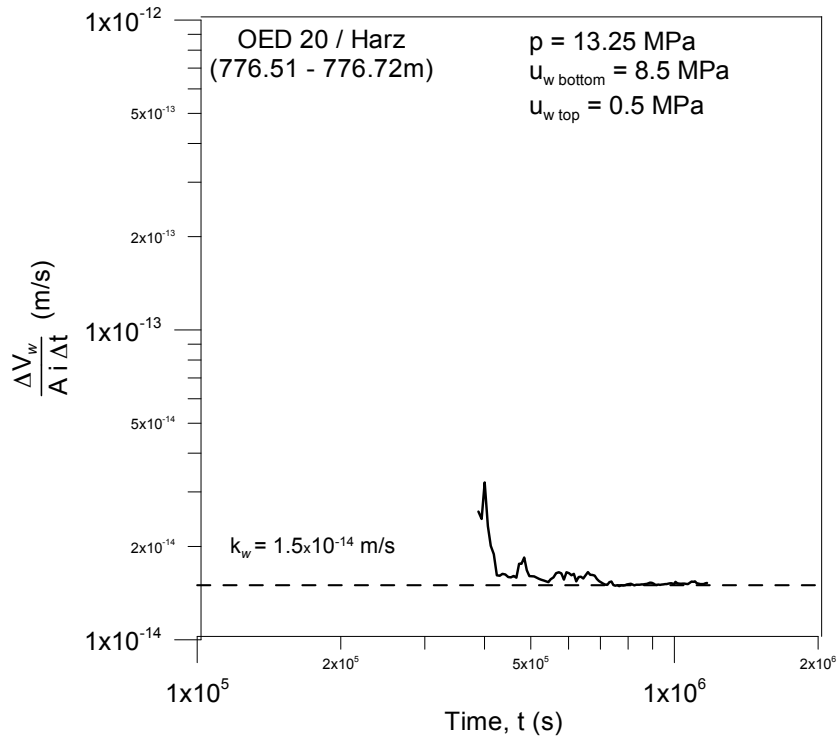


Fig. 3-13: Time evolution of $\Delta V_w / (A i \Delta t)$ under steady state conditions. Stage at $p = 13.25 \text{ MPa}$; $u_{w \text{ bottom}} = 8.5 \text{ MPa}$; $u_{w \text{ top}} = 0.5 \text{ MPa}$. OED 20/Harz 'Brown Dogger' sample.

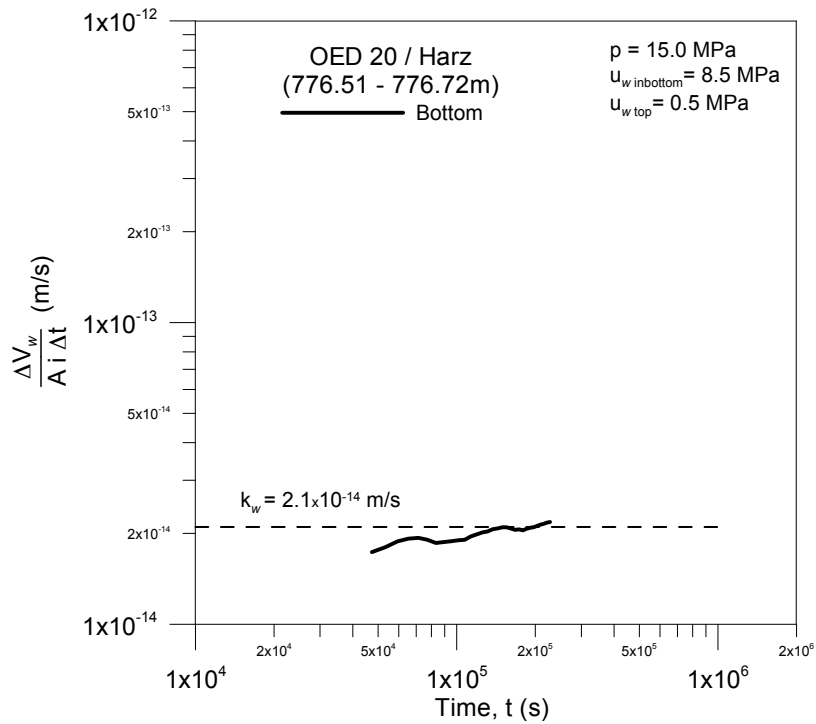


Fig. 3-14: Time evolution of $\Delta V_w / (A i \Delta t)$ under steady state conditions. Stage at $p = 15.0 \text{ MPa}$; $u_{w \text{ bottom}} = 8.5 \text{ MPa}$; $u_{w \text{ top}} = 0.5 \text{ MPa}$. OED 20/Harz 'Brown Dogger' sample.

OED Opalinus Clay (879.79 - 880.01 m) sample

Figure 3-15 to Figure 3-17 present the time evolution of water volume outflow (V_w) during three stages for water permeability determination reported in Table 3-1. In this case, only outflow volume was recorded.

Figure 3-18 to Figure 3-20 show the time evolutions in terms of $\Delta V_w / (A i \Delta t)$, where A is the sample cross-section, i the hydraulic gradient applied (Table 3-2), V_w the water volume flowing through the sample (measured as outflow volume), and t the elapsed time. Changes in volume and time are referred to a fixed initial value under steady state conditions (under steady state conditions, $\Delta V_w / (A i \Delta t)$ corresponds to water permeability k_w shown in the figures and summarised in Table 3-2).

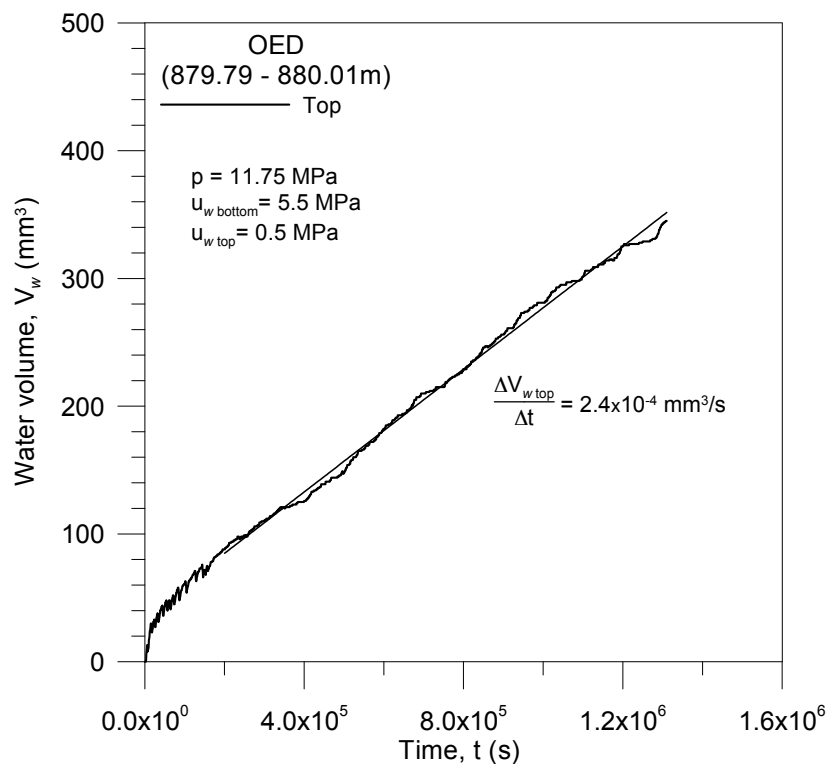


Fig. 3-15: Time evolution of water outflow volume. Stage at $p = 11.75 \text{ MPa}$; $u_{w\text{bottom}} = 5.5 \text{ MPa}$; $u_{w\text{top}} = 0.5 \text{ MPa}$. OED Opalinus Clay sample.

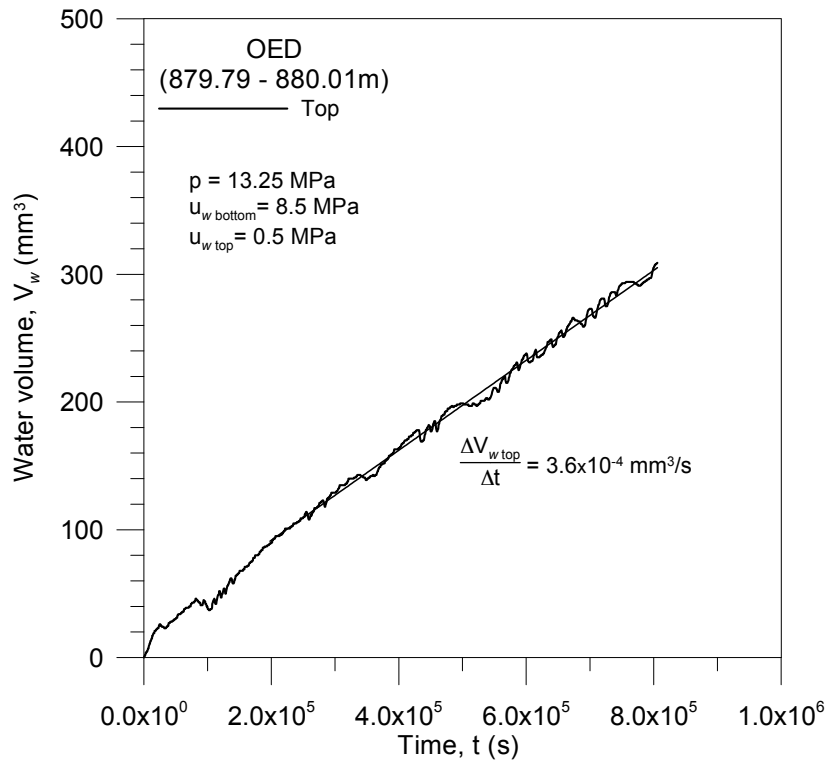


Fig. 3-16: Time evolution of water outflow volume. Stage at $p = 13.25$ MPa; $u_{w\text{bottom}} = 8.5$ MPa; $u_{w\text{top}} = 0.5$ MPa. OED Opalinus Clay sample.

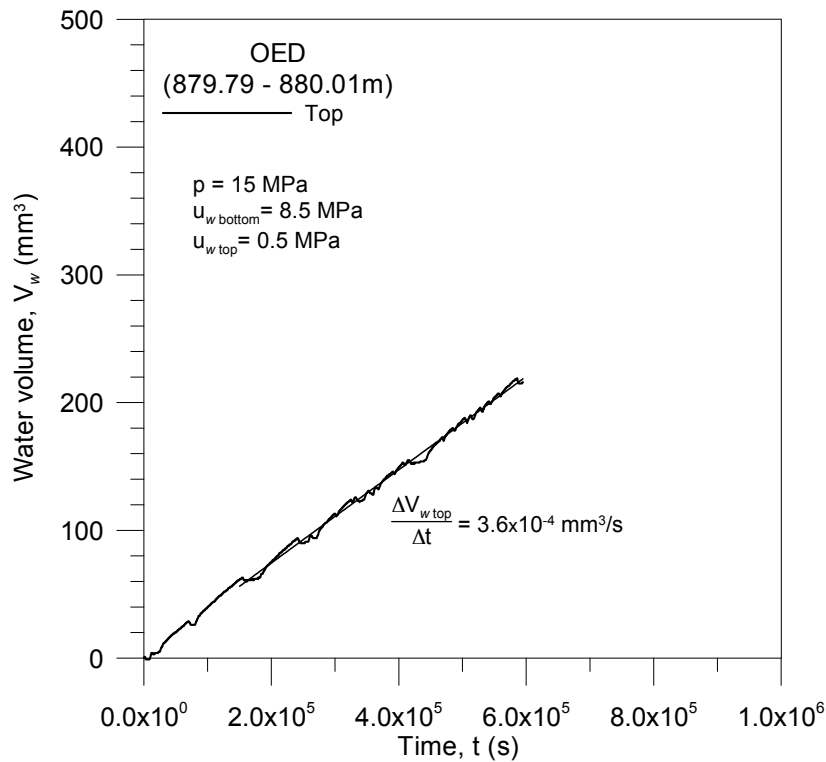


Fig. 3-17: Time evolution of water outflow volume. Stage at $p = 15.0$ MPa; $u_{w\text{bottom}} = 8.5$ MPa; $u_{w\text{top}} = 0.5$ MPa. OED Opalinus Clay sample.

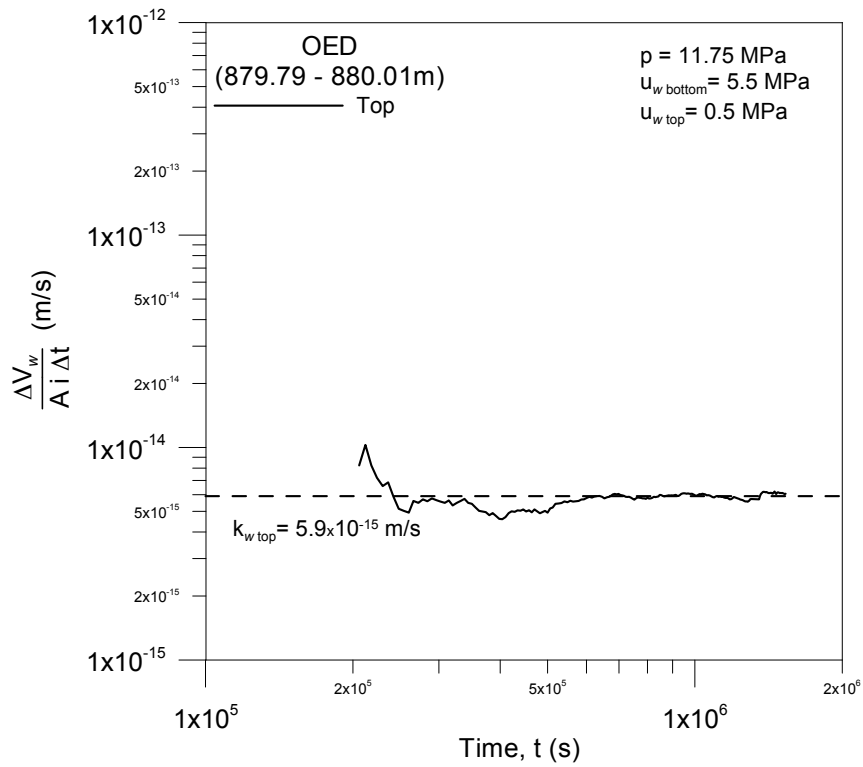


Fig. 3-18: Time evolution of $\Delta V_w / (A i \Delta t)$ under steady state conditions. Stage at $p = 11.75 \text{ MPa}$; $u_{w \text{ bottom}} = 5.5 \text{ MPa}$; $u_{w \text{ top}} = 0.5 \text{ MPa}$. OED Opalinus Clay sample.

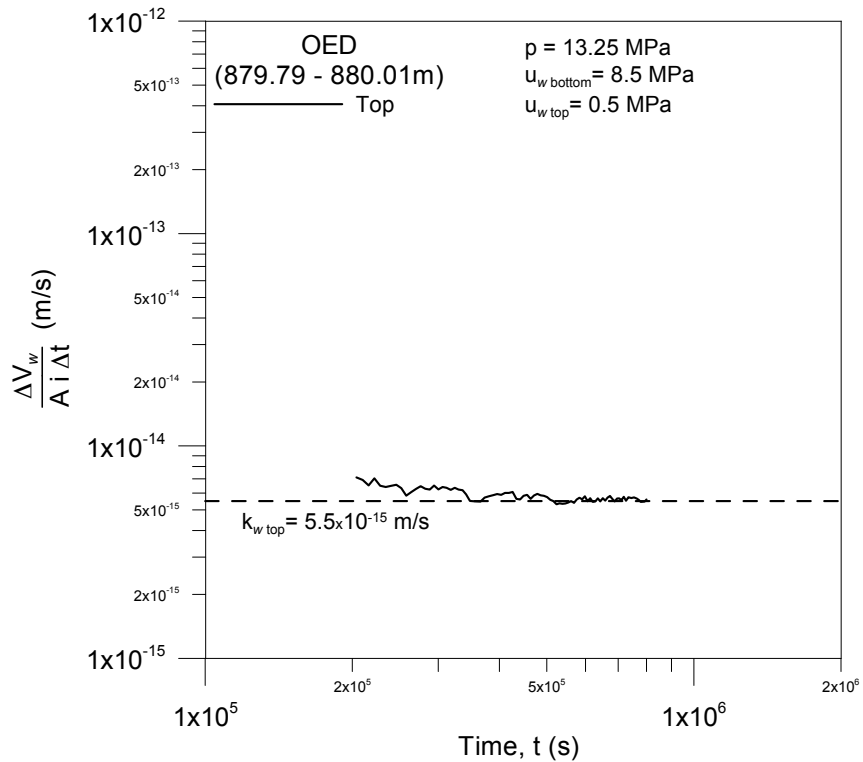


Fig. 3-19: Time evolution of $\Delta V_w / (A i \Delta t)$ under steady state conditions. Stage at $p = 13.25 \text{ MPa}$; $u_{w \text{ bottom}} = 8.5 \text{ MPa}$; $u_{w \text{ top}} = 0.5 \text{ MPa}$. OED Opalinus Clay sample.

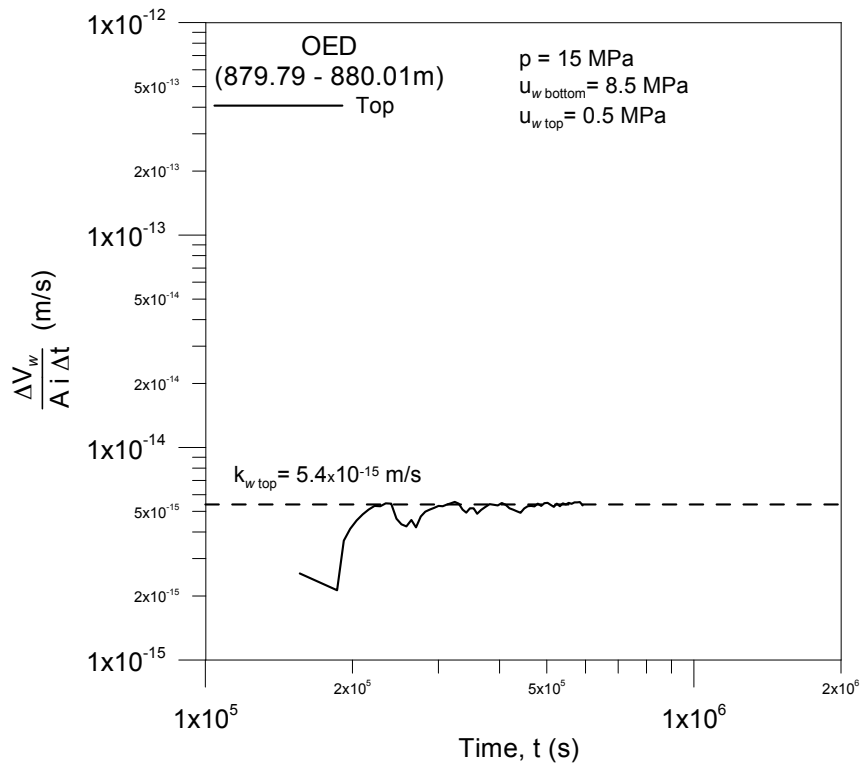


Fig. 3-20: Time evolution of $\Delta V_w / (A i \Delta t)$ under steady state conditions. Stage at $p = 15.0$ MPa; $u_{w\text{bottom}} = 8.5$ MPa; $u_{w\text{top}} = 0.5$ MPa. OED Opalinus Clay sample.

Water permeability results

Table 3-2 summarises the water permeability tests on OED 20/Harz 'Brown Dogger' (776.51 - 776.72 m) and OED Opalinus Clay (879.79 - 880.01 m) samples, where p is the isotropic total stress, u_w the water back pressure applied on bottom and top caps, i the hydraulic gradient, e the void ratio and k_w the water permeability. It also includes the intrinsic permeability K , considering a water property factor of $\rho_w g / \mu_w = 9.744 \times 10^6 \text{ (m.s)}^{-1}$ at 20°C (water density $\rho_w = 998.2 \text{ kg/m}^3$ and water dynamic viscosity $\mu_w = 1.005 \times 10^{-3} \text{ N.s/m}^2$).

Figure 3-21 shows the water permeability (flow perpendicular to bedding planes) as a function of void ratio of OED 20/Harz 'Brown Dogger' (776.51 - 776.72 m) and OED Opalinus Clay (879.79 - 880.01 m) samples. The figure also includes water permeability results for shallow OPA samples (OPA BHA-8/1 in the shaly facies, MI-niche; approx. 300 m depth), which is separated in water permeability with flow orthogonal and parallel to bedding planes. As shown in the figure, for constant void ratio, the anisotropy ratio K_{II}/K_{\perp} (ratio of intrinsic permeability parallel to flow to intrinsic permeability orthogonal to flow) is in the range 3 to 5. The clear measured dependency on void ratio has been fitted to the exponential equation indicated in the figure. The different parameters are included in the figure together with their respective fitted curves.

Tab. 3-2: Water permeability results.

| Stage | | | | OED 20/Harz 'Brown Dogger' (776.51 - 776.72 m) | | OED Opalinus Clay (879.79 - 880.01 m) | |
|--------------|------------------------|---------------------|--------------|--|--|---|--|
| p (MPa) | $u_{wbottom}$ (MPa) | u_{wtop} (MPa) | Gradient i | Void ratio e | k_w (m/s) K (m ²) | Void ratio e | k_w (m/s) K (m ²) |
| 10.0 | 2.0 | 0.5 | 6094 | 0.113 | 4.6×10^{-14} (4.7×10^{-21}) | 0.082 | 6.7×10^{-15} (6.8×10^{-22}) |
| 11.75 | 5.5 | 0.5 | 20312 | 0.109 | 2.3×10^{-14} (2.4×10^{-21}) | 0.078 | 5.9×10^{-15} (6.0×10^{-22}) |
| 13.25 | 8.5 | 0.5 | 32500 | 0.105 | 1.5×10^{-14} (1.6×10^{-21}) | 0.074 | 5.5×10^{-15} (5.6×10^{-22}) |
| 15.0 | 8.5 | 0.5 | 32500 | 0.101 | 2.1×10^{-14} (2.2×10^{-21}) | 0.070 | 5.4×10^{-15} (5.5×10^{-22}) |

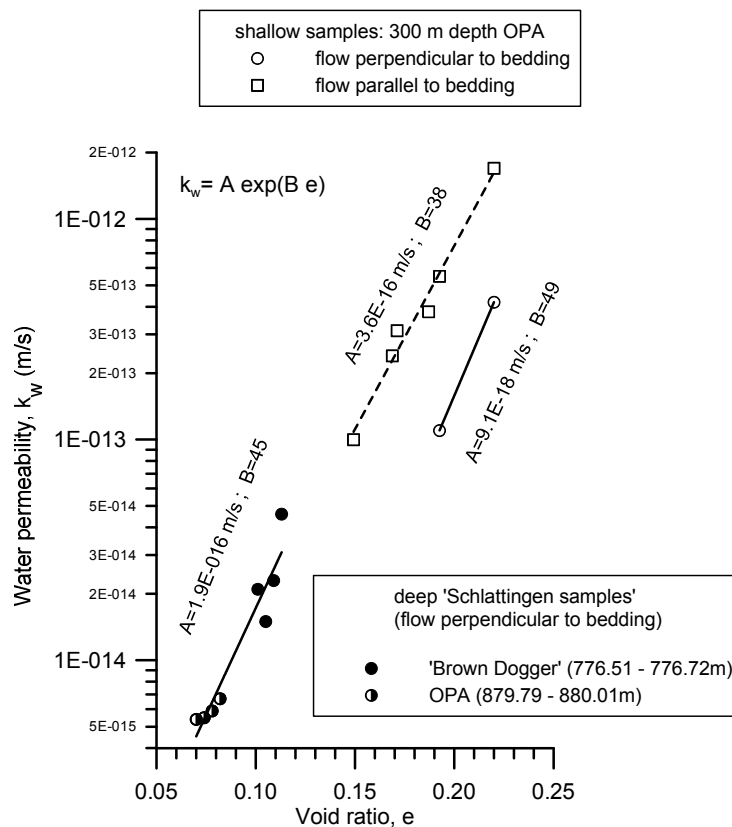


Fig. 3-21: Water permeability as a function of void ratio: OED 20/Harz (776.51 - 776.72 m) and OED (879.79 - 880.01 m) samples. Dependency on void ratio and orientation effects on shallow OPA samples.

Figure 3-22 shows water permeability results corresponding only to flow perpendicular to bedding planes for shallow and deep samples. The dependency has been fitted to a modified Kozeny-Carman equation:

$$k_w = A \frac{e^B}{(1+e)}$$

$$A = 1.09 \times 10^{-10} \text{ m/s}$$

$$B = 3.77$$
(4)

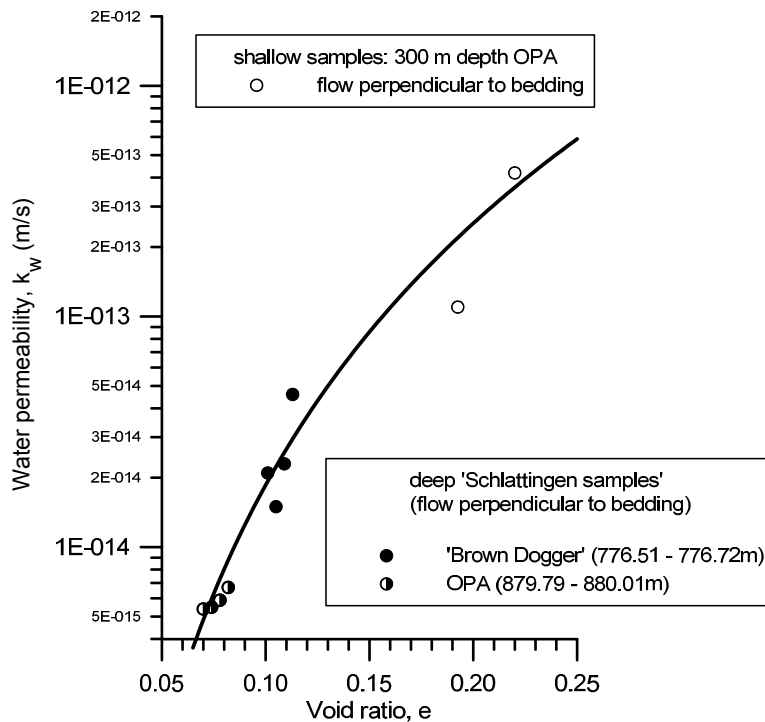


Fig. 3-22: Water permeability dependency on void ratio for flow perpendicular to bedding. 'Deep samples': OED 20/Harz (776.51 - 776.72 m) and OED (879.79 - 880.01 m). 'Shallow samples': OPA BHA-8/1 (approx. 300 m depth).

3.3 Air injection results

Previous results on shallow OPA samples

Figure 3-23 and Figure 3-24 show the time evolution of air injection pressure during fast controlled volume-rate tests (100 mL/min) at $p = 15$ MPa isotropic confining stress on 'shallow samples' (OPA BHA-8/1; approx. 300 m depth) under different orientations (air flow orthogonal to bedding –Test 1a–, and flow parallel to bedding –Test 1b–, respectively). V_0 in the figures represents the initial injection volume of air (injection piston around 500 mL and air inflow lines). This initial volume of air V_0 was fitted by considering a constant air mass system M_a during the initial stage of the fast injection process (least squares method applied to the difference S between measured absolute air injection \bar{u}_{ameas} and absolute air pressure estimated using perfect gas law \bar{u}_{aest} for given volume of air V at elapsed time t):

$$S = \sum_{i=1}^n (u_{a\text{meas}} - u_{a\text{est}})_i^2$$

$$\bar{u}_{a\text{est}} = \frac{M_a}{V M_{ma}} RT ; V = V_o - r t$$

$$M_{ma} \text{ (molecular mass of dry air mixture): } 28.966 \text{ kg/kmol} \quad (5)$$

$$R \text{ (universal molar gas constant): } 8.31432 \text{ J/(mol K)}$$

$$T = 295.15 \text{ K}$$

$$r = 100 \text{ mL/min (} t \text{: elapsed time)}$$

As observed in the figure, the injection pressure was able to increase to 12 and 13 MPa (depending on the test), followed by a shut-in and recovery period at constant volume. For the flow parallel to bedding (Figure 3-24), outflow response was immediately observed after shut-in corresponding to a drop in the injection pressure and followed by a subsequent gradual decline.

For the flow orthogonal to bedding (Figure 3-23), the injection pressure remained initially flat and the outflow response was significantly delayed indicating also anisotropy during air permeability tests. After the apparent air breakthrough process corresponding to an increase in the outflow pressure, the injection pressure showed a steep decline. The constant downstream pressure condition of 0.5 MPa was not possible to maintain due to the high outflow volume rates detected (the downstream pressure increased until reaching 2 MPa, where a constant pressure was again prescribed by the pressure release valve).

With regard to the axial displacement response (negative axial displacements and strains corresponds to expansion), the samples at constant isotropic total stress displayed expansion at the early fast air injection stage and progressive compression on air pressure dissipation (Fig. 3-25). As a first approximation, this behavioural feature at constant isotropic total stress has been associated with pore pressure changes inducing constitutive (effective) stress variations: pore pressure increase inducing mean effective stress decrease (and thus expansion), followed by compression due to mean effective stress increase (pore pressure dissipation stage). The axial strain response during air tests with flow orthogonal and parallel to bedding is plotted in terms of constitutive stress changes (estimated as the isotropic stress p minus the air pressure at the injection point u_a). Three different stages are indicated in the figure for the evolution of the axial strains: a) an initial expansion during the fast injection stage due to constitutive stress decrease (AB in the figure); b) an expansion before the air breakthrough process (BC at the initial part of the shut-in stage), and c) a final compression stage during the recovery period at increasing constitutive stress. As shown in the figure, a stiffer response on air pressure dissipation is obtained compared to the loading / unloading stages reported in Table 3-1 for the deeper samples (bulk stiffness is calculated assuming no significant radial straining). If these volumetric strain changes (around 0.20%) are solely interpreted as changes in pore volume (void ratio changes around 0.002), then changes in intrinsic permeability are expected to be small (refer to Table 3-2). Other mechanisms, such as opening of discontinuities, have been suggested (see for instance, Olivella & Alonso 2008) to enhance intrinsic permeability changes.

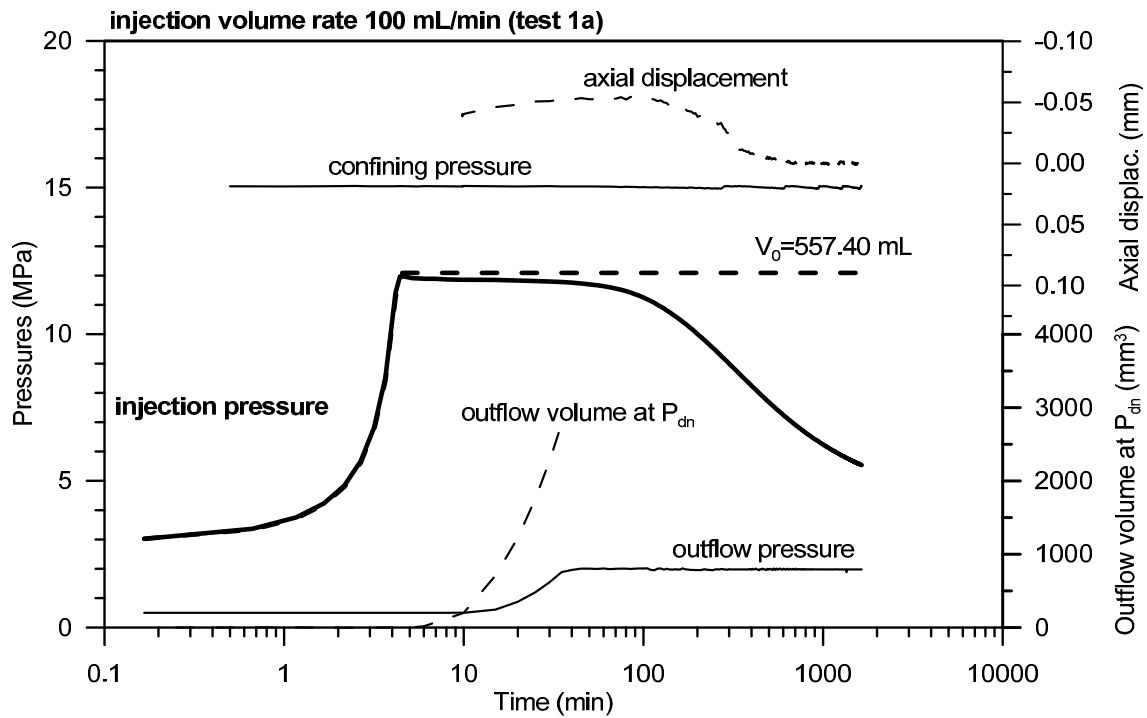


Fig. 3-23: Measured time evolution of pressures at the injection and outflow sides together with outflow volume and axial displacements. OPA shallow sample with bedding plane orientation orthogonal to flow at $p = 15$ MPa.

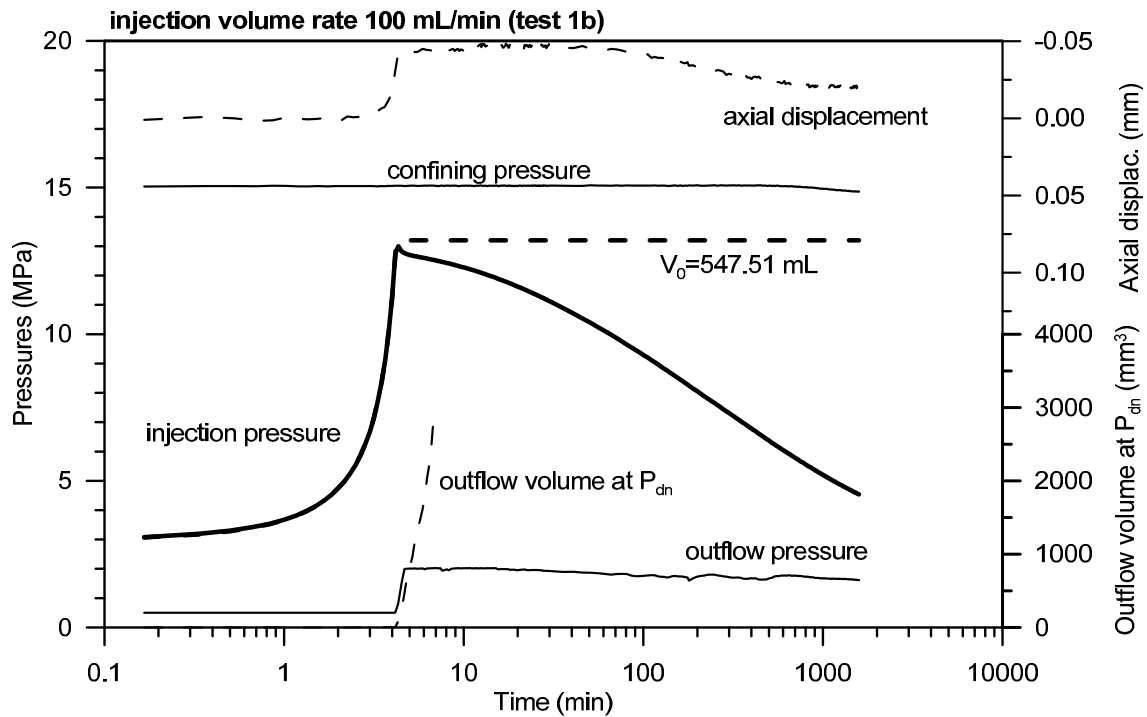


Fig. 3-24: Measured time evolution of pressures at the injection and outflow sides together with outflow volume and axial displacements. 'Shallow sample' with bedding plane orientation parallel to flow at $p = 15$ MPa.

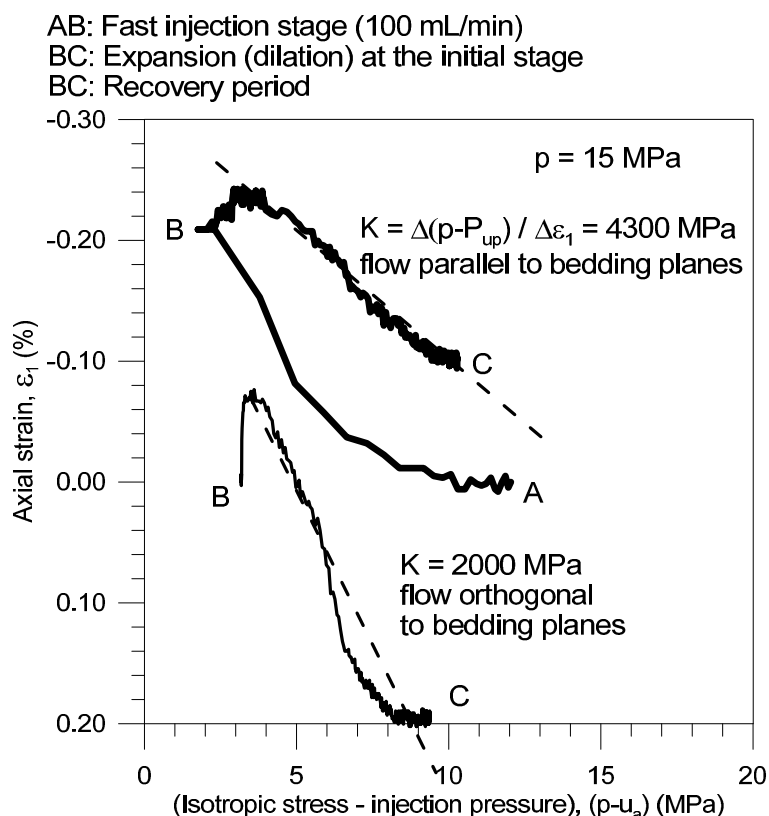


Fig. 3-25: Axial strain changes associated with constitutive (effective) stress changes during air tests with flow parallel and orthogonal to bedding.

Results on OED 20/Harz 'Brown Dogger' (776.51 - 776.72 m) sample

Figure 3-26 presents the air injection results for the low-permeability OED 20/Harz 'Brown Dogger' (776.51 - 776.72 m) sample at $p = 15 \text{ MPa}$ isotropic confining stress, when air injection pressure is increased to 14 MPa at a rate of 100 mL/min. This maximum air pressure is around the estimated air-entry value from MIP reported in Table 2-2. The initial injection volume of air (injection piston around 500 mL and air inflow lines) is indicated in the figure. In this case, the injection pressure essentially remained flat in the recovery stage at constant volume without appreciable outflow volume detected (the outflow pressure remained at 0.5 MPa). The outflow volume slightly increased after 8000 min, when a steeper decline was recorded for the air pressure in the recovery stage. The evolution of the axial deformation is also presented in the figure.

Figure 3-27 shows the equivalent time evolution of air injection pressure, axial displacement, as well as outflow volume and pressure at downstream under a higher isotropic stress of $p = 19 \text{ MPa}$ on the same material. In this case, the injection air pressure increased to a value slightly larger (18 MPa) than the estimated air-entry value by MIP (Table 2-2), and the air injection pressure after shut-in dissipated at a faster rate. In this case, the initial volume V_0 (injection piston around 350 mL and air inflow lines) is lower due to some problems detected in the pressure volume controller. The outflow volume slightly increased after 300 min, when a consistent steeper decline was recorded for the air pressure in the recovery stage. Despite the faster dissipation rate, the outflow pressure was able to be maintained at 0.5 MPa. The evolution of the axial deformation is also presented in the figure.

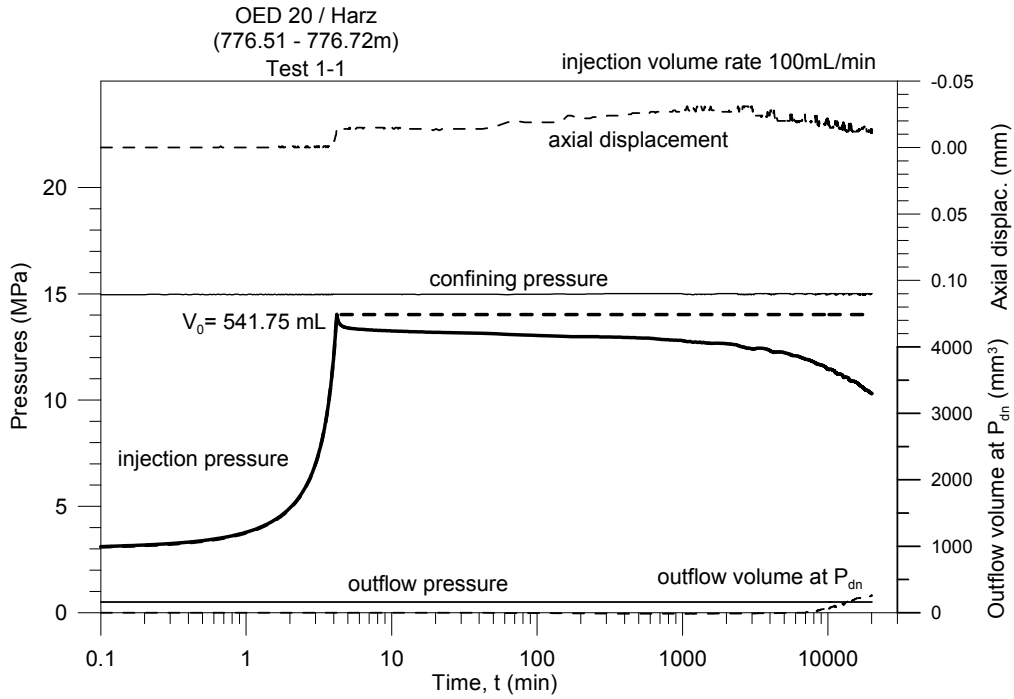


Fig. 3-26: Measured time evolution of pressures at the injection and outflow sides together with outflow volume and axial displacements. OED 20/Harz 'Brown Dogger' (776.51 - 776.72 m) sample with flow orthogonal to bedding plane orientation at $p = 15 \text{ MPa}$.

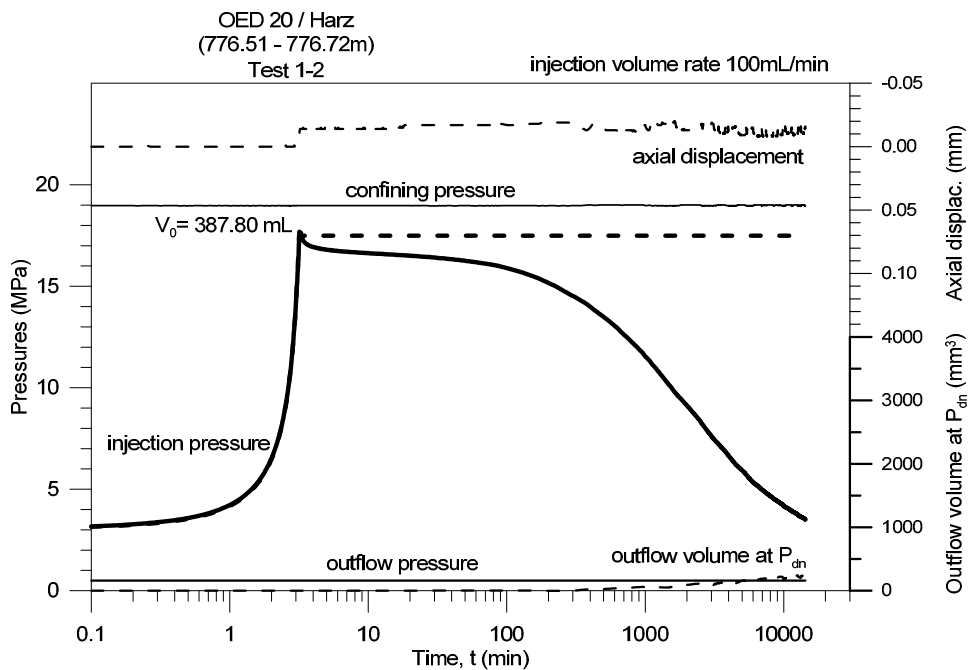


Fig. 3-27: Measured time evolution of pressures at the injection and outflow sides together with outflow volume and axial displacements. OED 20/Harz 'Brown Dogger' (776.51 - 776.72 m) sample with flow orthogonal to bedding plane orientation at $p = 19 \text{ MPa}$.

Results on OED Opalinus Clay (879.79 - 880.01 m) sample

Figure 3-28 shows the air injection results for the low-permeability OED Opalinus Clay (879.79 - 880.01 m) sample at $p = 15$ MPa isotropic confining stress, when air injection pressure is increased to 14 MPa at a rate of 100 mL/min. This maximum air pressure is below the estimated air-entry value from MIP reported in Table 2-3 (around 18 MPa). The initial injection volume of air (injection piston around 500 mL and air inflow lines) is indicated in the figure. The injection pressure remained initially flat in the recovery stage and a steeper decline was recorded after 1000 min (earlier than the equivalent test performed on 'Brown Dogger', Figure 3-23). Despite its lower intrinsic permeability (Table 3-2), the material underwent higher air dissipation rates during the recovery stage compared to the equivalent test performed on 'Brown Dogger', Figure 3-23). Nevertheless, outflow volume was only recorded after 7000 min, probably due to some problems in the downstream pressure / volume controller. Outflow pressure always remained at 0.5 MPa. The evolution of the axial deformation is also presented in the figure.

Figure 3-29 shows the equivalent time evolution of air injection pressure, axial displacement, as well as outflow volume and pressure at downstream under a higher isotropic stress of $p = 19$ MPa on the same material. The injection air pressure increased to a value (18 MPa) close to estimated air-entry value by MIP (Table 2-3). Consequently, the air injection pressure after shut-in dissipated at a faster rate -particularly at elapsed times higher than 50 min-, reaching a final value below 3 MPa. Again, outflow volume was only recorded after 7000 min, probably due to some problems in the downstream pressure / volume controller. Outflow pressure remained at 0.5 MPa. The evolution of the axial deformation is also presented in the figure.

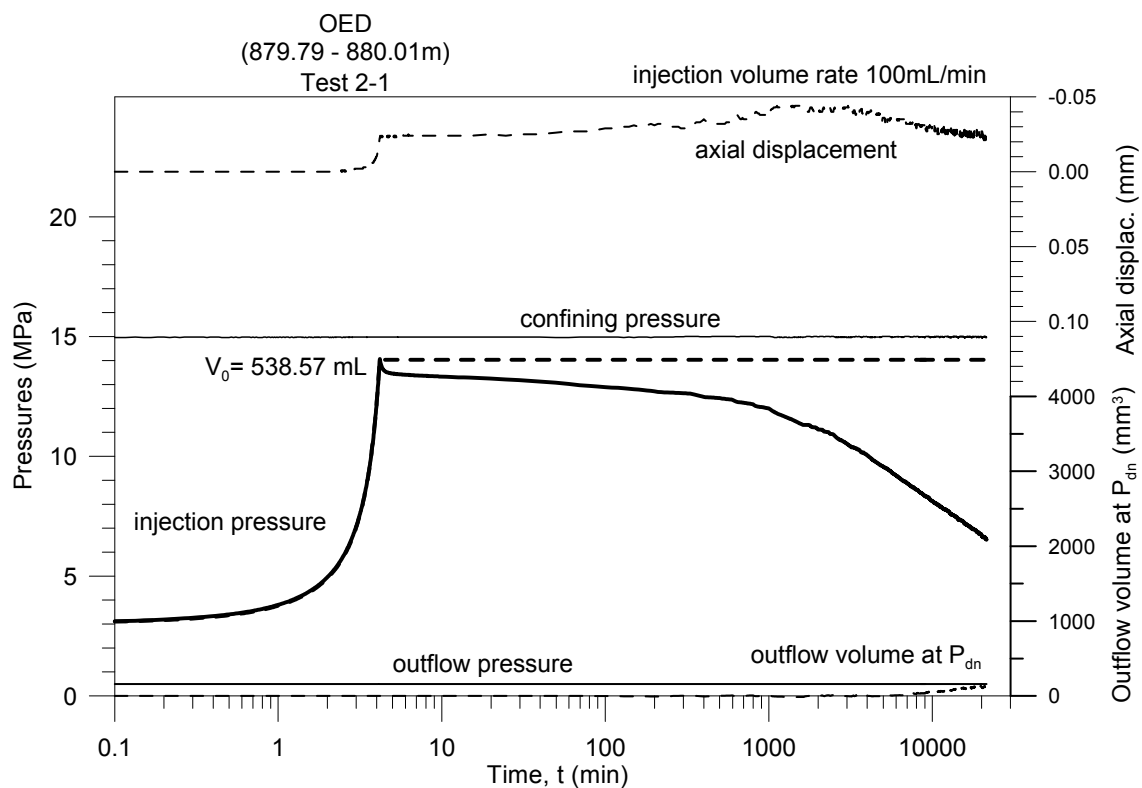


Fig. 3-28: Measured time evolution of pressures at the injection and outflow sides together with outflow volume and axial displacements. OED Opalinus Clay (879.79 - 880.01 m) sample with flow orthogonal to bedding plane orientation at $p = 15$ MPa.

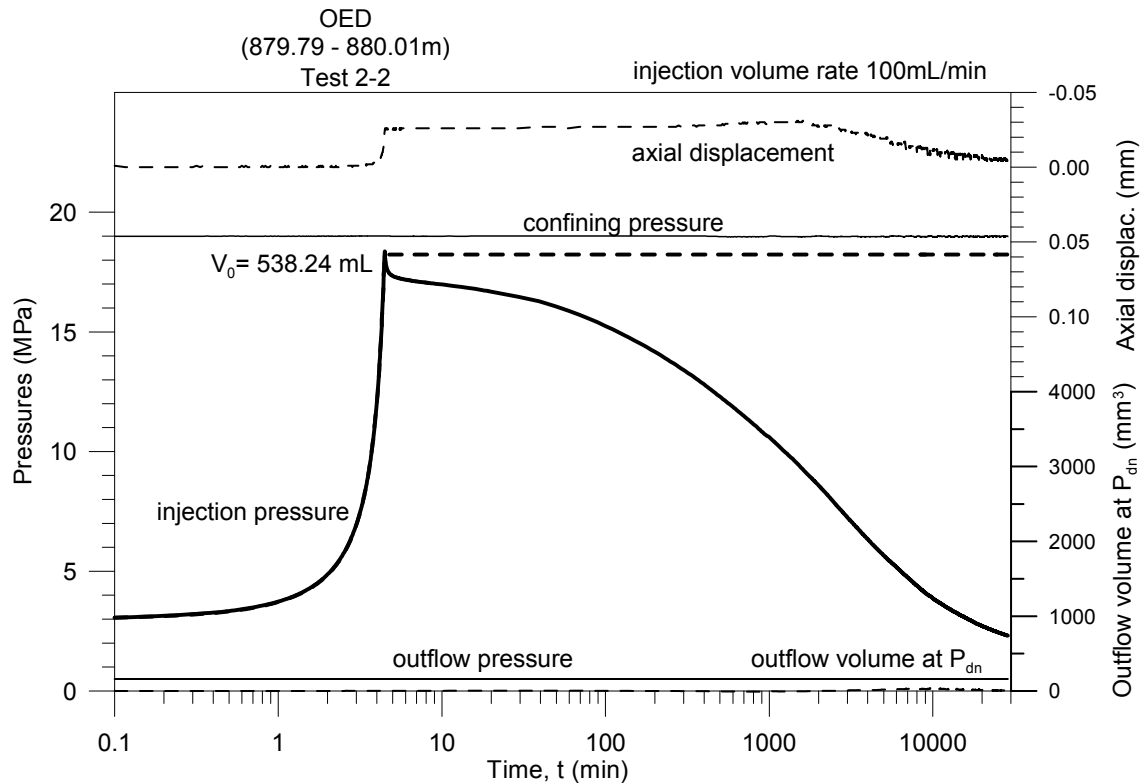


Fig. 3-29: Measured time evolution of pressures at the injection and outflow sides together with outflow volume and axial displacements. OED Opalinus Clay (879.79 - 880.01 m) sample with flow orthogonal to bedding plane orientation at $p = 19$ MPa.

With regard to the axial displacement response (negative axial displacements and strains corresponds to expansion), Figure 3-30 shows its evolution during the air injection tests on Opalinus Clay and 'Brown Dogger' samples at $p = 15$ MPa and $p = 19$ MPa, respectively. The axial strains are plotted in terms of constitutive stress changes (estimated as the isotropic stress p minus the air pressure at the injection point u_a). Again, the examination of the axial strains revealed different deformation stages. The initial air pressure increase (AB in the figure) associated with a decrease in the constitutive (effective) stress indicates expansion of the sample. During the early period after shut-in (BC in the figure), the air pressure slightly decreased -increase in constitutive stress-, but the axial strain continued to expand (between -0.05% and -0.10%). Afterwards, the axial strain reversed indicating compression as the constitutive stress increased during air pressure dissipation (around 0.10% during the last phase BC). As shown in the figure, a stiffer response is obtained in this dissipation phase compared to the loading / unloading stages reported in Table 3-1 (bulk stiffness is calculated assuming no significant radial straining).

The axial displacement response at 19 MPa (Figure 3-30b) shows a similar response as the response at 15 MPa, except that the axial strain increase during expansion stage (“BC”) is less distinct.

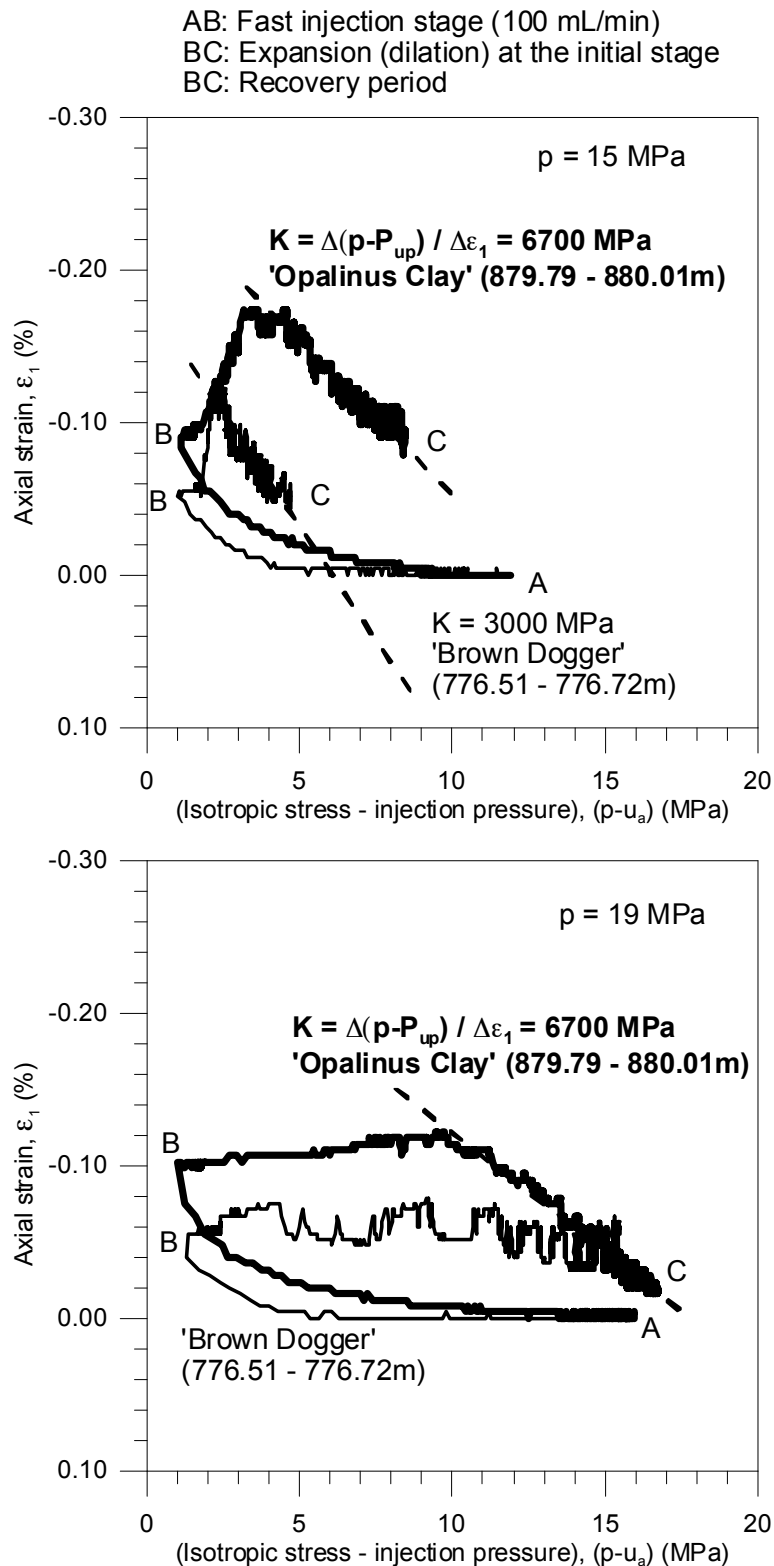


Fig. 3-30: Axial strain changes associated with constitutive (effective) stress changes during air tests with flow orthogonal to bedding. Samples of OED Opalinus Clay (879.79 - 880.01 m) and OED 20/Harz 'Brown Dogger' (776.51 - 776.72 m) at (a) $p = 15$ MPa and (b) $p = 19$ MPa.

4 Summary and Conclusions

The document describes the geotechnical characterisation, experimental setup and procedures for long-term water and air permeability tests performed on two low-permeability clay-rich samples retrieved from the Schlattingen/Thurgau borehole (Switzerland) at two different depths (776.5 m depth / 'Brown Dogger' and 879.9 m depth / Opalinus Clay).

The geotechnical characterisation included the definition of the initial state of the tested materials with particular emphasis on the pore size distribution with mercury intrusion porosimetry / nitrogen adsorption, the water retention properties on drying and the compressibility on isotropic loading / unloading paths.

Some effort was also done in improving the experimental setup using an instrumented high-pressure triaxial cell, which was specifically updated to apply higher isotropic stress states, while injecting air at controlled-volume rate up to a maximum pressure of 18 MPa. Careful sample preparation protocols were also followed to prepare the samples.

Long-term water permeability tests at different effective stress states and hydraulic gradients were performed that allowed accounting for the change in intrinsic permeability with void ratio. Tests were run with flow orthogonal to bedding planes.

The main stage of the program was devoted to study the influence of the stress state under isotropic conditions on the air permeability of initially water saturated samples. Four controlled-volume rate air injection tests followed by shut-in and air pressure pulse decay stages were run with flow orthogonal to bedding planes. Two different maximum air injection pressures were attained at fast and constant air injection rate (100 mL/min) before shut-in and air dissipation. The maximum air injection pressures were in one case below the air-entry value determined by MIP and around the air-entry value in the second case. Particular emphasis was placed in monitoring sample volume changes (axial strains) during air injection and dissipation stages.

The water and air permeability experiments showed clear evidence for the important dependency of water permeability on void ratio and thus on constitutive stress. The deeper Opalinus Clay samples, which presented slightly lower void ratios (refer to Table 2-3), consistently displayed lower water permeability values (Figure 3-22). Nevertheless, despite its lower intrinsic permeability, the Opalinus Clay samples underwent slightly higher air dissipation rates during the recovery stage compared to the equivalent tests performed on 'Brown Dogger'. Higher air dissipation rates were consistently measured after shut-in, when higher air pressures were applied during air injection (close to the estimated air-entry values).

Another important observation is the axial displacement of the tested samples in response to the increase / decrease in air pressure, suggesting a marked dependency of volumetric strain on the constitutive stress changes during air injection / dissipation tests, as well as on air-driven opening / closure of discontinuities. The samples displayed expansion at the early fast air injection stage in response to constitutive stress decrease, and dominant compression on air pressure dissipation. Nevertheless, during the early period after shut-in, the axial strain continued to expand despite the slight increase in constitutive stress due to air dissipation. This phenomenon occurs under increasing amount of air stored in the sample before the development of air-driven opening of discontinuities (dilatational pathways in zones with initially closed or with low aperture fractures, and in zones where fractures are developed if certain conditions are attained). In addition, higher bulk moduli were consistently obtained in the air dissipation phases compared to bulk moduli from loading and unloading stages.

These observations highlight the importance of carefully carrying out volume change determinations (axial and radial strains) along the injection, shut-in and dissipation stages, since the different deformation regimes can be associated with different mechanisms that are affecting the gas transport and rock mechanical and hydraulic properties (e.g.; air-driven opening of discontinuities and stress-strain response affecting flow parameters; fracturing associated with air pathways inducing rock degradation).

The detailed analyses of the laboratory experiments will be helpful in the development of conceptual and numerical models for simulating two-phase flow of gas through a low-permeability clay formation, in which relevant information on sample volume changes and associated changes in intrinsic permeability should be taken into consideration. In this context, new experimental tests on deep clay formations have been initiated with significantly lower gas pressure build-up rates to better understand the different deformation regimes and their associated mechanisms, as well as their impact on gas transport, mechanical and hydraulic properties.

5 References

- Albert, W., H.R. Bläsi, H. Madritsch, T. Vogt, H.P. Weber (2012): Geologie, Stratigraphie, Strukturgeologie, bohrlochgeophysikalisches Logging und Wasserproben der Geothermiebohrung Schlattingen SLA-1 (Rohdaten). Nagra Project Report NPB 12-16, Nagra, Wettingen, Switzerland.
- Cardoso R., Romero E., Lima A. & Ferrari A. (2007). A comparative study of soil suction measurement using two different high-range psychrometers. Proc. 2nd Int. Conf. Mechanics of Unsaturated Soils, Weimar, Germany, March 7-9, 2007. Experimental Unsaturated Soil Mechanics. T. Schanz (ed.). Springer Proceedings in Physics, 112. Springer-Verlag, Berlin: 79-93.
- Mazurek, M. (2011): Aufbau und Auswertung der Gesteinsparameter-Datenbank für Opalinuston, den 'Braunen Dogger', Effinger Schichten und Mergel-Formationen des Helvetikums. Nagra Arbeitsbericht NAB 11-20. Nagra, Wettingen.
- Olivella S. & Alonso E.E. (2008). Gas flow through clay barriers. *Géotechnique* 58(3): 157-176.
- Pineda J.A., Romero E., Alonso E.E. & Pérez T. (submitted). A new high-pressure triaxial apparatus for inducing and tracking hydro-mechanical degradation of clayey rocks. Submitted to *Geotechnical Testing Journal*.
- Romero E. (1999). Characterisation and thermo-hydro-mechanical behaviour of unsaturated Boom clay: an experimental study. PhD Thesis. Universitat Politècnica de Catalunya, Spain. <http://hdl.handle.net/10803/6224>.
- Romero E. & Simms P.H. (2008). Microstructure investigation in unsaturated soils: A review with special attention to contribution of mercury intrusion porosimetry and environmental scanning electron microscopy. *Geotechnical and Geological Engineering* 26(6): 705-727, doi: 10.1007/s10706-008-9204-5.
- Romero E., Musso G. & Jommi C. (2012a). Experimental techniques for multi-scale description of soil fabric and its dual pore network. In: ALERT Doctoral School 2012 'Advanced experimental techniques in geomechanics'. G. Viggiani, S.A. Hall and E. Romero (eds.). ALERT Geomaterials, France: 125-156. <http://hdl.handle.net/2117/18773>.
- Romero, E., Senger, R. and Marschall, P. (2012b). Air Injection laboratory experiments on Opalinus clay. Experimental techniques, results and analyses. *Proceedings 3rd Shale Workshop EAGE Conferences*, Barcelona, Spain, January 23-25, 2012. C07: 96-100.
- Romero, E., Senger, R., Marschall, P., and Gómez, R. (2012c). Air tests on low-permeability claystone formations. Experimental results and simulations. Theme lecture. *Int. Workshop 'AMTSS - Advances in Multiphysical Testing of Soils and Shales'*, EPFL Lausanne (Switzerland), September 3-5, 2012. In: *Multiphysical Testing of Soils and Shales*. L. Laloui & A. Ferrari (eds.). Springer-Verlag, Berlin: 68-83.
- Senger, R., Romero, E., Ferrari, A. and Marschall, P. (2012). Characterization of gas flow through low-permeability claystone. Laboratory experiments and two-phase flow analyses. *Clays in Natural and Engineered Barriers for Radioactive Waste Confinement, 4th International Meeting Andra* (France), Montpellier, France, 22-25 October, 2012. Book of abstracts, Edited by Andra, Nagra, Ondraf and SKB: 700-701.

- Senger, R., Romero, E., Ferrari, A. and Marschall, P. (submitted). Characterization of gas flow through low-permeability claystone: Laboratory experiments and two-phase flow analyses. Submitted for publication in a volume of the 'Geological Society Special Publication series' (GeolSoc books).
- van Genuchten, M.Th. (1980). A closed-form equation for predicting the hydraulic conductivity of unsaturated soils. *Soil Science Society of America Journal* 44(5): 892-898.
- Webb, P.A. & Orr, C. (1997). Analytical methods in fine particle technology. Micromeritics Instrument Corp, Norcross, GA, USA.

Appendix A – Structure of the electronic data base

Overview

Auxiliary digital files containing the whole set of data were made available to NAGRA. The electronic data base ensures the traceability of the reported raw data and the results of data analyses and collects all graphical data representations. The electronic data base is organized in the 2 main directories:

| | | |
|---|------------------|-------------|
|  0 Report NAB12-51_UPC-SLA-1 | 28.06.2013 08:51 | Dateiordner |
|  1 Data_NAB12-50_UPC-SLA-1 | 28.06.2013 08:47 | Dateiordner |
|  2 Related Papers | 28.06.2013 08:49 | Dateiordner |

The data needed to create the diagrams of the experimental results in the report are provided in an EXCEL file in the directory "1 Data NAB12-51_UPC-SLA-1":

| | | | |
|--|------------------|-----------------------|----------|
|  data_figures_def.xls | 28.06.2013 10:25 | Microsoft Excel 97... | 2'649 KB |
|--|------------------|-----------------------|----------|

Several presentations and papers which are directly related to the experimental results of this report are appended in "2 Related Papers":

| | | | |
|---|------------------|---------------------|----------|
|  04 Romeroetal_Gasinjection_Nantes2010... | 30.03.2010 10:22 | Microsoft PowerP... | 7'726 KB |
|  AMTSS_Romero_etal_Shale_092012_3.pdf | 10.09.2012 10:37 | Adobe Acrobat D... | 6'829 KB |
|  Romero et al AMTSS_2012_airtests.pdf | 26.05.2012 09:05 | Adobe Acrobat D... | 314 KB |
|  SessionIII_C07_Romero_etal_ShaleWorksh... | 30.01.2012 21:06 | Adobe Acrobat D... | 1'264 KB |